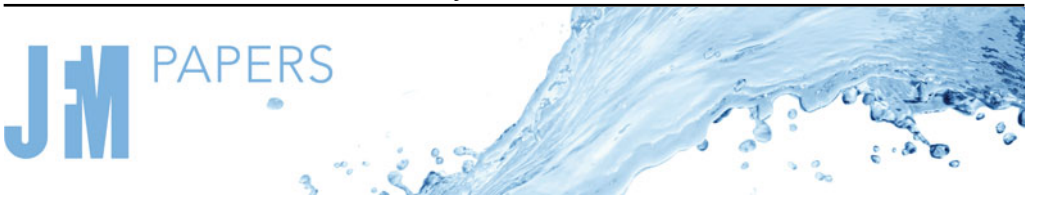
J. Fluid Mech. (2026), *vol.* 1027, A5, doi:10.1017/jfm.2025.11022



Data-driven detached-eddy simulations based on explicit algebraic stress expressions for turbulent flows

Hao-Chen Liu[1,2], **Zifei Yin**[3], **Xin-Lei Zhang**[1,2] **and Guowei He**[1,2]

[1]The State Key Laboratory of Nonlinear Mechanics, Institute of Mechanics, Chinese Academy of Sciences, Beijing 100190, PR China

[2]School of Engineering Sciences, University of Chinese Academy of Sciences, Beijing 100049, PR China

[3]School of Aeronautics and Astronautics, Shanghai Jiao Tong University, Shanghai 200240, PR China

Corresponding authors: Guowei He, hgw@lnm.imech.ac.cn; Xin-Lei Zhang, zhangxinlei@imech.ac.cn

(Received 21 June 2025; revised 23 September 2025; accepted 1 December 2025)

This work proposes a data-driven explicit algebraic stress-based detached-eddy simulation (DES) method. Despite the widespread use of data-driven methods in model development for both Reynolds-averaged Navier–Stokes (RANS) and large-eddy simulations (LES), their applications to DES remain limited. The challenge mainly lies in the absence of modelled stress data, the requirement for proper length scales in RANS and LES branches, and the maintenance of a reasonable switching behaviour. The data-driven DES method is constructed based on the algebraic stress equation. The control of RANS/LES switching is achieved through the eddy viscosity in the linear part of the modelled stress, under the $\ell^2 - \omega$ DES framework. Three model coefficients associated with the pressure–strain terms and the LES length scale are represented by a neural network as functions of scalar invariants of velocity gradient. The neural network is trained using velocity data with the ensemble Kalman method, thereby circumventing the requirement for modelled stress data. Moreover, the baseline coefficient values are incorporated as additional reference data to ensure reasonable switching behaviour. The proposed approach is evaluated on two challenging turbulent flows, i.e. the secondary flow in a square duct and the separated flow over a bump. The trained model achieves significant improvements in predicting mean flow statistics compared with the baseline model. This is attributed to improved predictions of the modelled stress. The trained model also exhibits reasonable switching behaviour, enlarging the LES region to resolve more turbulent structures. Furthermore, the model shows satisfactory generalization capabilities for both cases in similar flow configurations.

Key words: machine learning, turbulence modelling

© The Author(s), 2026. Published by Cambridge University Press.

https://doi.org/10.1017/jfm.2025.11022 Published online by Cambridge University Press

1. Introduction

Hybrid Reynolds-averaged Navier–Stokes/large eddy simulation (RANS/LES) methods are of practical interest for efficiently predicting massively separated flows in industrial applications (Chaouat 2017; Heinz 2020). These approaches typically employ the RANS models within the near-wall attached boundary layers and switch to LES in the outer flow, thereby offering a favourable compromise between computational cost and predictive accuracy. The detached-eddy simulation (DES) (Spalart 2009) is one of the most widely used hybrid approaches, which enables automatic switching from RANS to LES within a unified turbulence model. This is achieved by defining the effective length scale as the minimum between the RANS-based integral scale ℓ_{RANS} and the LES-based subgrid scale ℓ_{LES} (typically proportional to the cell size). As a result, when the local mesh resolution is sufficiently fine to resolve the associated turbulent structures, the LES mode is activated such that the modelled stress is constrained to be the subgrid-scale stress.

The first DES model, proposed by Spalart (1997), enables resolving turbulent structures away from walls by bounding the required wall distance d in the Spalart–Allmaras turbulence model using the scaled local cell size, i.e. $d^* = \min(d, C_{DES}\Delta)$. This original DES model primarily suffers from two weaknesses: grid-induced separation (GIS) and log-layer mismatch (LLM) (Spalart 2009). To alleviate the GIS problem, Spalart *et al.* (2006) developed the delayed-DES (DDES) model that uses a shielding function to maintain the RANS model behaviour near-walls. Furthermore, Shur *et al.* (2008) proposed the improved DDES (IDDES) model, which introduces additional blending functions to enable wall-modelled LES behaviour within boundary layers when the mesh quality allows. Meanwhile, the LLM issue is mitigated by redefining the subgrid-scale Δ to enable a similar behaviour as the Smagorinsky model on the LES branch.

Alternatively, Reddy, Ryon & Durbin (2014) proposed the $\ell^2 - \omega$ DDES model, offering a relatively simple yet effective framework. Specifically, the eddy viscosity in this model is defined using the DDES length scale ℓ_{DDES} as $\nu_t = \ell_{DDES}^2\omega$, which results in an eddy viscosity behaviour that closely resembles the Smagorinsky model in the LES branch. As such, the underlying DDES framework can ensure the RANS mode in the near-wall region, avoiding the GIS issue. On the other hand, the LLM deficiency can be mitigated by redefining the subgrid-scale Δ as the cubic root of the cell volume in the LES region, similar as the IDDES model (Shur *et al.* 2008) but with a simpler definition of Δ. Furthermore, the adaptive version of the $\ell^2 - \omega$ DDES model is proposed (Yin, Reddy & Durbin 2015; Yin & Durbin 2016; Bader, Yin & Durbin 2022), where the DES coefficient C_{DES} is dynamically computed based on the Germano identity (Lilly 1991) or the Vreman kernel (Vreman 2004). This advancement significantly broadens the applicability of DES across a wide range of flow configurations (Yin, Ge & Durbin 2021; Yin & Durbin 2022; Liu *et al.* 2024*a*).

Besides these contributions, numerous extensions and enhancements to the DES method have been explored in the literature (Deck 2012; Gritskevich *et al.* 2012; Ashton *et al.* 2013; Le Pape, Richez & Deck 2013; Jee & Shariff 2014; Han, He & Le 2020; Pont-Vílchez *et al.* 2021; Liu *et al.* 2024*c*). However, most existing DES models are still based on linear eddy viscosity (LEV) RANS models. These models often struggle to provide reliable predictions in complex flows characterized by strong Reynolds stress anisotropy, such as rotating flows, secondary flows and flows over curved surfaces (Durbin 2018).

In view of this shortcoming, Liu *et al.* (2024*b*) proposed the explicit algebraic stress-based DDES (EAS-DDES) model. The modelled stress, denoting the Reynolds stress on the RANS branch and the subgrid stress on the LES branch, is decomposed into a linear and a nonlinear part. The linear part takes charge of the switching between the RANS

https://doi.org/10.1017/jfm.2025.11022 Published online by Cambridge University Press

and LES branches based on the $\ell^2 - \omega$ DDES framework. The nonlinear part accounts for the modelled stress anisotropy, which is formulated based on the explicit algebraic Reynolds stress (EARS) of Wallin & Johansson (2000). This enables the EAS-DDES model to outperform the LEV-DES models in complex turbulent flows, particularly when near-wall stress anisotropy becomes pronounced (Liu *et al.* 2024*b*). In addition, the EAS-DDES model can achieve better computational efficiency, stability and robustness than the Reynolds stress transport-based DES approaches (Zhuchkov & Utkina 2016; Liu *et al.* 2021; Wang, Li & Liu 2021; Li *et al.* 2022) due to the explicit algebraic stress formulation.

The EAS-DDES model is built based on the EARS model of Wallin & Johansson (2000). There exist several model coefficients that are determined from canonical turbulent flows. Specifically, the coefficient values in the pressure–strain rate term of the algebraic stress equation are adopted from Taulbee (1992) and Wallin & Johansson (2000), which is determined based on homogeneous shear flow (Harris, Graham & Corrsin 1977). For other types of turbulent flows, the model coefficients can be calibrated to provide better predictions (Pope 2000). Also, the coefficient C_{DES} controls the magnitude of the subgrid stress, the standard value of which is determined based on the Smagorinsky constant. It has been shown that the adaptive adjustment of C_{DES} according to the local turbulent state provides superior performance in various flow cases (Yin *et al.* 2015). Therefore, determining these model coefficients based on local features is promising for further improving the predictive performance of the EAS-DDES model.

Over the past decade, the rapid advancement of data-driven approaches has paved the way for developing predictive turbulence models directly from high-fidelity data (Duraisamy, Iaccarino & Xiao 2019; Brunton, Noack & Koumoutsakos 2020; Duraisamy 2021; Sandberg & Zhao 2022). Various data-driven methods have been employed to develop RANS turbulence models, including adjoint-based methods (Singh, Medida & Duraisamy 2017), decision tree algorithms (Matai & Durbin 2019*a*), sparse regression (Schmelzer, Dwight & Cinnella 2020), gene expression programming (Fang *et al.* 2023), random forest (Volpiani 2024) and so on. Particularly, the ensemble Kalman method (Evensen 2009) has also been applied to train the neural network-based Reynolds stress models (Zhang *et al.* 2022, 2023*a*,*b*). This method enables the efficient training of a neural network-based model coupled with the RANS solver, thereby avoiding inconsistencies between the training and prediction environments (Duraisamy 2021). Moreover, the data requirement is significantly relaxed, as only measurable flow quantities, such as sparse measurements of mean velocities, are needed, rather than full-field Reynolds stress.

Besides the applications in RANS models, data-driven methods are also emerging for the LES in building subgrid stress models and wall models (Duraisamy 2021). Early works mainly focus on subgrid stress modelling of canonical turbulent flows, such as the isotropic turbulence (Sirignano, MacArt & Freund 2020) and channel flow (Park & Choi 2021; Xu *et al.* 2023). Further, Sirignano & MacArt (2023) trained a subgrid stress model for bluff-body separation flows using adjoint-based methods, showing significant improvement in predictive accuracy over traditional models. The data-driven method has also been applied to build neural network-based wall models (Zhou *et al.* 2021, 2025). Particularly, Lozano-Durán & Bae (2023) proposed a neural network-based building-block-flow wall model, which has been applied to two realistic aircraft configurations. More recently, Zhang *et al.* (2025) proposed a knowledge-integrated additive learning approach for learning LES wall models, the predictive capability of which has been demonstrated in channel flows, separated flows over periodic hills and the two-dimensional Gaussian bump.

Despite the widespread use of data-driven methods in the development of both RANS and LES models, their application to the DES remains limited. The primary challenges of the data-driven DES stem from three key aspects. The first is the absence of a

https://doi.org/10.1017/jfm.2025.11022 Published online by Cambridge University Press

benchmark database for modelled stress. In data-driven RANS modelling, the target data of Reynolds stress is the second-order moments of the velocity fluctuations. In data-driven LES modelling, the target data of subgrid stress is also accessible from the filtered direct numerical simulation (DNS). However, in a DES simulation, the switching process from RANS to LES trades the modelled and the resolved stresses. No instantaneous, explicit 'optimal' switching from RANS to LES can be derived. As such, the local proportion of the total stress to be resolved and modelled is unknown and cannot be obtained from DNS or experimental measurements.

Given that DES is intrinsically an automatic length scale formulation, the second challenge is to ensure the proper length scales for the model to choose from. Specifically, a too low RANS length scale in the region away from the wall may cause the LES subgrid viscosity to be wrongly suppressed when resolving eddies. Correspondingly, a spuriously low LES length scale in the near-wall region would also cause modelled stress depletion, which may lead to GIS or LLM issues (Spalart 2009). It is a new constraint for data-driven modelling because no previous practice requires consideration of how the model would perform when an 'LES' solution is fed to a data-driven RANS model, and *vice versa*.

The third challenge lies in maintaining a seamless and stable switching between RANS and LES branches, particularly in flows for which the model has not been trained. The RANS-to-LES interface continuously evolves at each time step during the simulation. Ideally, it should become stabilized within a certain range of wall distance, regardless of the initial condition. However, as the data-driven model is trained statistically on certain flow types, its generalizability in maintaining proper interface location is difficult to guarantee. Drifting away from the ideal interface location during the unsteady time-marching can lead to LLM or even become a pure RANS or coarse-grid LES. It remains an open issue in the hybrid RANS/LES modelling community to achieve seamless switching between RANS and LES. And it is even more challenging in data-driven DES modelling, given the nonlinear nature and the indirect tuning of the coefficients of neural networks.

The present study aims to propose a framework for building a data-driven DES model based on the algebraic stress equation. To the authors' knowledge, this is the first such attempt in data-driven turbulence modelling for the DES. A physically reasonable and mathematically consistent expression of the modelled stress in RANS and LES branches is constructed through the algebraic stress approach under the weak-equilibrium assumption. The switching between the RANS and LES branches is achieved through the eddy viscosity, or equivalently, turbulent kinetic energy (TKE). The neural network is used to represent the functional mapping from the local flow features to the model coefficients. The neural network is trained using the ensemble Kalman method, which enables model training with mean velocity data from experiments or high-fidelity simulations, thereby avoiding the requirement for modelled stress data. The reasonable length scales and switching behaviours are enforced by augmenting the training data with the baseline values of the model coefficients, which can ensure similar behaviours to the baseline model.

The rest of this paper is organized as follows. The general expression of the modelled stress in DES based on the algebraic stress modelling approach is established in § 2. The data-driven closure of the model coefficients, including the neural network-based model representation and the ensemble Kalman method for model training, is introduced in § 3. The capability of the present data-driven explicit algebraic stress DDES (DD-EAS-DDES) approach in predicting complex turbulent flows, specifically the secondary flow in a square duct and the separated flow over a bump, is demonstrated in §§ 4 and 5, respectively. The generalizability of the present model is also illustrated. The physical consistency and training efficiency of the present approach are further discussed in § 6. Finally, § 7 concludes the entire work.

https://doi.org/10.1017/jfm.2025.11022 Published online by Cambridge University Press

2. Modelling framework

2.1. Governing equations

The governing equations for the EAS-DDES model (Liu *et al.* 2024*b*) read as

$$\begin{aligned}
&\nabla\cdot\bar{\boldsymbol{u}}=0,\\
&\frac{D\bar{\boldsymbol{u}}}{Dt}=-\nabla\bar{p}+\nabla\cdot(\nu\nabla\bar{u})-\nabla\cdot\boldsymbol{\tau},\\
&\frac{Dk}{Dt}=-\boldsymbol{\tau}:\bar{\boldsymbol{S}}-C_\mu k\omega+\nabla\cdot\left[\left(\nu+\frac{C_\mu^*\sigma_k}{C_\mu}\frac{k}{\omega}\right)\nabla k\right],\\
&\frac{D\omega}{Dt}=\frac{2C_{\omega1}C_\mu^*}{C_\mu}|\bar{S}|^2-C_{\omega1}\omega\boldsymbol{a}^*:\bar{\boldsymbol{S}}-C_{\omega2}\omega^2+\nabla\cdot\left[\left(\nu+\frac{C_\mu^*\sigma_\omega}{C_\mu}\frac{k}{\omega}\right)\nabla\omega\right],
\end{aligned}\tag{2.1}$$

where p denotes the pressure normalized by the constant flow density, $\boldsymbol{u}$ is the velocity, ν is the kinetic viscosity, k is the TKE, ω is the turbulence frequency, C_μ is the standard eddy viscosity coefficient, C_μ^* represents the effective C_μ and $\bar{\boldsymbol{S}}$ denotes the strain rate tensor as

$$\bar{\boldsymbol{S}}\equiv\frac{1}{2}\left[\nabla\bar{\boldsymbol{u}}+(\nabla\bar{\boldsymbol{u}})^T\right].\tag{2.2}$$

Here, the RANS ensemble-average and the LES spatial-filtering are collectively denoted by the overline $(\bar{\cdot})$. The standard values of the model constants are adopted as $C_\mu=0.09$, $\sigma_k=\sigma_\omega=0.5$, $C_{\omega1}=5/9$, $C_{\omega2}=3/40$.

The modelled stress $\boldsymbol{\tau}$ is expressed as (Liu *et al.* 2024*b*)

$$\boldsymbol{\tau}\equiv\overline{\boldsymbol{u}\boldsymbol{u}}-\bar{\boldsymbol{u}}\bar{\boldsymbol{u}}=k\boldsymbol{a}+\frac{2}{3}k\boldsymbol{I}=-2\nu_t\bar{\boldsymbol{S}}+k\boldsymbol{a}^*+\frac{2}{3}k\boldsymbol{I}.\tag{2.3}$$

In the EAS-DDES model, the linear part $(-2\nu_t\bar{S})$ directly controls the switching between the RANS and LES branches through the eddy viscosity ν_t, and the nonlinear part $\boldsymbol{a}^*$ reacts to that, adding the extra anisotropy to the modelled stress. In the following, the modelling of the linear and nonlinear parts of the turbulent stress is illustrated, respectively.

2.2. Modelling of the linear part in the DDES manner

The linear part of the turbulent stress is modelled by following the $\ell^2-\omega$ DDES framework (Reddy *et al.* 2014). Specifically, the eddy viscosity ν_t in the linear part is calculated as

$$\nu_t=\ell_{DDES}^2\omega.\tag{2.4}$$

The DDES length scale ℓ_{DDES} calculated from the RANS and LES length scales (ℓ_{RANS} and ℓ_{LES}) as

$$\ell_{DDES}=\ell_{RANS}-f_d\max(0,\ell_{RANS}-\ell_{LES}),\tag{2.5}$$

where

$$\begin{aligned}
&\ell_{RANS}=\sqrt{\frac{C_\mu^*}{C_\mu}}\frac{\sqrt{k}}{\omega},\quad \ell_{LES}=C_{DES}\Delta,\\
&\Delta=f_dV^{1/3}+(1-f_d)\,h_{max}.
\end{aligned}\tag{2.6}$$

Here V is the local cell volume, and h_{max} is the local maximum cell spacing in the three directions. The shielding function f_d is to ensure the near-wall RANS region, which is

https://doi.org/10.1017/jfm.2025.11022 Published online by Cambridge University Press

formulated as

$$f_d = 1 - \tanh[(8r_d)^3], \quad r_d = \frac{(C_\mu^*/C_\mu)k/\omega + \nu}{\kappa^2 d_w^2 \sqrt{\nabla \bar{\boldsymbol{u}} : \nabla \bar{\boldsymbol{u}}}} \tag{2.7}$$

with κ being the von Kármán constant, and d_w the wall distance.

2.3. *General expression of the nonlinear part*

As for the nonlinear extra anisotropy $\boldsymbol{a}^*$, the most general expression is adopted as (Pope 1975)

$$\boldsymbol{a}^* = \sum_{i=2}^{10} \beta_i \boldsymbol{T}_i, \tag{2.8}$$

which is derived under the effective-viscosity hypothesis and the Cayley–Hamilton theorem. Here $\boldsymbol{T}_i$ are the tensor basis as

$$\begin{aligned}
&\boldsymbol{T}_2 = \boldsymbol{S}^2 - \frac{1}{3}\theta_1 \boldsymbol{I}, \quad \boldsymbol{T}_3 = \boldsymbol{\Omega}^2 - \frac{1}{3}\theta_2 \boldsymbol{I}, \quad \boldsymbol{T}_4 = \boldsymbol{S\Omega} - \boldsymbol{\Omega S}, \\
&\boldsymbol{T}_5 = \boldsymbol{S}^2\boldsymbol{\Omega} - \boldsymbol{\Omega S}^2, \quad \boldsymbol{T}_6 = \boldsymbol{S\Omega}^2 + \boldsymbol{\Omega}^2\boldsymbol{S} - \frac{2}{3}\theta_4 \boldsymbol{I} - \theta_2 \boldsymbol{S}, \\
&\boldsymbol{T}_7 = \boldsymbol{S}^2\boldsymbol{\Omega}^2 + \boldsymbol{\Omega}^2\boldsymbol{S}^2 - \frac{2}{3}\theta_5 \boldsymbol{I} - \theta_4 \boldsymbol{S}, \quad \boldsymbol{T}_8 = \boldsymbol{S\Omega S}^2 - \boldsymbol{S}^2\boldsymbol{\Omega S}, \\
&\boldsymbol{T}_9 = \boldsymbol{\Omega S\Omega}^2 - \boldsymbol{\Omega}^2\boldsymbol{S\Omega}, \quad \boldsymbol{T}_{10} = \boldsymbol{\Omega S}^2\boldsymbol{\Omega}^2 - \boldsymbol{\Omega}^2\boldsymbol{S}^2\boldsymbol{\Omega},
\end{aligned} \tag{2.9}$$

with $\boldsymbol{I}$ being the identity matrix. The tensor coefficients β_i depend on the five invariants as

$$\theta_1 = \mathrm{tr}(\boldsymbol{S}^2), \quad \theta_2 = \mathrm{tr}(\boldsymbol{\Omega}^2), \quad \theta_3 = \mathrm{tr}(\boldsymbol{S}^3), \quad \theta_4 = \mathrm{tr}(\boldsymbol{S\Omega}^2), \quad \theta_5 = \mathrm{tr}(\boldsymbol{S}^2\boldsymbol{\Omega}^2). \tag{2.10}$$

The normalized strain and rotation rates are defined as

$$\boldsymbol{S} \equiv \frac{\nabla \bar{\boldsymbol{u}} + (\nabla \bar{\boldsymbol{u}})^T}{2C_\mu \omega}, \quad \boldsymbol{\Omega} \equiv -\frac{\nabla \bar{\boldsymbol{u}} - (\nabla \bar{\boldsymbol{u}})^T}{2C_\mu \omega}. \tag{2.11}$$

Note that the tensor bases $\boldsymbol{T}_6$ and $\boldsymbol{T}_7$ differ from the original expressions of Pope (1975) in the existence of the last terms. This is due to the extraction of the linear components, which are absorbed into the linear part of the modelled stress. Accordingly, C_μ^* is expressed as

$$C_\mu^* = -\frac{1}{2}(\beta_1 + \theta_2\beta_6 + \theta_4\beta_7) \tag{2.12}$$

where β_1 represents the coefficient of the first tensor basis $\boldsymbol{T}_1 = \boldsymbol{S}$ in the general expression of $\boldsymbol{a}$.

2.4. *Closure through the algebraic stress equation*

To close the tensor basis coefficients β_i, the algebraic stress modelling framework is adopted under the weak-equilibrium assumption. The transport of the modelled stress $\boldsymbol{\tau}$ can be considered to be due to transports in k and modelled stress anisotropy $\boldsymbol{a}$. The former is retained, while the latter is neglected (Pope 2000), resulting in an implicit algebraic equation of $\boldsymbol{a}$ as

$$\left(\boldsymbol{a} + \frac{2}{3}\boldsymbol{I}\right)(\mathcal{P} - \varepsilon) = \boldsymbol{P} - \boldsymbol{E} + \boldsymbol{\Pi}, \tag{2.13}$$

https://doi.org/10.1017/jfm.2025.11022 Published online by Cambridge University Press

where the production tensor $\boldsymbol{P}$ is in closed form as

$$\boldsymbol{P} \equiv -\boldsymbol{\tau}\nabla\bar{\boldsymbol{u}} - (\nabla\bar{\boldsymbol{u}})^T\boldsymbol{\tau} = \varepsilon\left(-\frac{4}{3}\boldsymbol{S} - \boldsymbol{a}\boldsymbol{S} - \boldsymbol{S}\boldsymbol{a} + \boldsymbol{a}\boldsymbol{\Omega} - \boldsymbol{\Omega}\boldsymbol{a}\right), \tag{2.14}$$

and $\mathcal{P} \equiv \mathrm{tr}(\boldsymbol{P})/2$. For the dissipation tensor $\boldsymbol{E}$, lumping the dissipation anisotropy into the pressure–strain rate tensor $\boldsymbol{\Pi}$ results in (Pope 2000)

$$\boldsymbol{E} = \frac{2}{3}\varepsilon\boldsymbol{I}. \tag{2.15}$$

The pressure–strain rate tensor $\boldsymbol{\Pi}$ can be decomposed into a slow and a rapid component, i.e. $\boldsymbol{\Pi}^s$ and $\boldsymbol{\Pi}^r$, respectively. The Rotta model (Rotta 1951) is used for $\boldsymbol{\Pi}^s$ as

$$\boldsymbol{\Pi}^s = -C_1\varepsilon\boldsymbol{a}, \tag{2.16}$$

representing a linear return to isotropy of the Reynolds stress. The Rotta constant C_1 determines the rate of return to isotropy. As for the rapid pressure–strain rate $\boldsymbol{\Pi}^r$, there exist several models (Pope 2000). Here we follow Taulbee (1992) and Wallin & Johansson (2000) to adopt the general linear model of Launder, Reece & Rodi (1975) for $\boldsymbol{\Pi}^r$ as

$$\boldsymbol{\Pi}^r = -\frac{C_2+8}{11}\left(\boldsymbol{P} - \frac{2}{3}\mathcal{P}\boldsymbol{I}\right) - \frac{60C_2-4}{55}\varepsilon\boldsymbol{S} - \frac{8C_2-2}{11}\left(\boldsymbol{D} - \frac{2}{3}\mathcal{P}\boldsymbol{I}\right), \tag{2.17}$$

where

$$\boldsymbol{D} \equiv -\boldsymbol{\tau}(\nabla\bar{\boldsymbol{u}})^T - (\nabla\bar{\boldsymbol{u}})\boldsymbol{\tau} = \varepsilon\left(-\frac{4}{3}\boldsymbol{S} - \boldsymbol{a}\boldsymbol{S} - \boldsymbol{S}\boldsymbol{a} - \boldsymbol{a}\boldsymbol{\Omega} + \boldsymbol{\Omega}\boldsymbol{a}\right). \tag{2.18}$$

Inserting (2.14)–(2.18) into (2.13), the algebraic equation for the modelled stress anisotropy tensor $\boldsymbol{a}$ is derived as

$$\left(C_1 - 1 + \frac{\mathcal{P}}{\varepsilon}\right)\boldsymbol{a} = -\frac{8}{15}\boldsymbol{S} + \frac{7C_2+1}{11}(\boldsymbol{a}\boldsymbol{\Omega} - \boldsymbol{\Omega}\boldsymbol{a}) - \frac{5-9C_2}{11}\left[\boldsymbol{a}\boldsymbol{S} + \boldsymbol{S}\boldsymbol{a} - \frac{2}{3}\mathrm{tr}(\boldsymbol{a}\boldsymbol{S})\boldsymbol{I}\right], \tag{2.19}$$

where

$$\mathcal{P}/\varepsilon \equiv -\mathrm{tr}(\boldsymbol{a}\boldsymbol{S}). \tag{2.20}$$

The above algebraic stress equation is a nonlinear equation of $\boldsymbol{a}$ due to (2.20). Wallin & Johansson (2000) obtained the approximated solution by inserting the general form of $\boldsymbol{a}$ as (2.8) into (2.19). The resulting linear system of β_i can then be formulated as functions of $\mathcal{P}/\varepsilon$, C_1, C_2 and θ_j by assuming that $\mathcal{P}/\varepsilon$ is already determined. Then $\mathcal{P}/\varepsilon$ is solved by inserting the solution of $\boldsymbol{a}$ into (2.20). In doing so, the functions of $\beta_i(C_1, C_2; \theta_j)$ can be obtained. The full expressions of the tensor coefficients β are provided in Appendix A. The neglect of the advection and diffusion of $\boldsymbol{a}$ under the weak equilibrium assumption may cause problems in flows where the production-to-dissipation ratio is small, leading to overestimated C_μ^*. Given this, an effective diffusion term is added as a correction in such cases (Wallin & Johansson 2000). The details are also provided in Appendix A. As such, the present general EAS-DDES model is obtained, provided with the pressure–strain rate coefficients C_1, C_2 and the DES coefficient C_{DES}.

Note that the algebraic equation (2.19) of $\boldsymbol{a}$ is consistent for both the Reynolds stress and the subgrid stress. Although the extra correlation terms $\overline{\overline{\boldsymbol{S}}p'}$ exist in the pressure–strain rate tensor due to the filtering process, $\boldsymbol{\Pi}$ can be modelled in a similar way for both the Reynolds stress and the subgrid stress as (2.16) and (2.17) (Marstorp *et al.* 2009).

https://doi.org/10.1017/jfm.2025.11022 Published online by Cambridge University Press

Hence, (2.19) and its solution $\beta_i(C_1, C_2; \theta_i)$ are mathematically consistent in both the RANS and eddy-resolving regions, for the hybrid RANS/LES methods.

The present EAS-DDES framework is based on the weak-equilibrium assumption (Rodi 1972), where the convection and diffusion of the anisotropy $\boldsymbol{a}$ are neglected. Hence, the variation of the Reynolds stress is attributed solely to the modelled kinetic energy, k, i.e.

$$\frac{D\boldsymbol{\tau}}{Dt} - \boldsymbol{T} \approx \frac{\boldsymbol{\tau}}{k}\left(\frac{Dk}{Dt} - T_k\right) \tag{2.21}$$

where $\boldsymbol{T}$ is the diffusion of modelled stress and $T_k = (1/2)\,\mathrm{tr}(\boldsymbol{T})$ is the diffusion of k. In the DES method, the switching of k from the TKE in the RANS branch to subgrid kinetic energy is achieved by the suppression of ν_t, which consequently affects the production term in the transport equation of k. Therefore, the modelled stress can be naturally switched from the Reynolds stress to the subgrid stress under the weak-equilibrium assumption, leading to a consistent form of the modelled stress anisotropy $\boldsymbol{a}$ in RANS and LES branches.

Admittedly, an algebraic stress model under the weak-equilibrium assumption cannot fully represent transport effects like a full differential Reynolds stress model. However, it offers a significant improvement over LEV models by capturing anisotropy effects. The algebraic closure of the modelled stress anisotropy $\boldsymbol{a}$ provides a reasonable compromise between the computational cost and physical accuracy for many practically relevant flows (Gatski & Jongen 2000; Durbin 2018).

For the baseline EAS-DDES model (Liu *et al.* 2024*b*), the coefficients $C_1 = 1.8$ and $C_2 = 5/9$ are set by following Wallin & Johansson (2000), and the coefficient $C_{DES} = 0.12(C_\mu^*/C_\mu)^{-1/4}$ is set to ensure the same subgrid stress intensity as the Smagorinsky model with the Smagorinsky constant $C_S = 0.2$. The last term in (2.19) vanishes at $C_2 = 5/9$, and the solution of β_i is largely simplified due to $\beta_{2,5,7,8,10} = 0$. In the next section, we introduce the data-driven method to learn the neural network-based closure of these coefficients.

3. Data-driven closure of the model coefficients

As described in § 2, the general EAS-DDES model is closed with the model coefficients C_1, C_2 and C_{DES} determined. Although the baseline model (Liu *et al.* 2024*b*) provides a set of coefficients, it is of significant interest to optimize the coefficient set for further predictive improvement. For the pressure–strain rate coefficients C_1 and C_2, various combinations have been employed in previous studies, and the optimal set of coefficients is found to differ across various cases (Pope 2000). In addition, the modelled stress anisotropies at the RANS integral scale and the LES subgrid scale are inherently different, requiring different sets of C_1 and C_2 on the RANS and LES branches. This is evident in the explicit algebraic subgrid stress model of Marstorp *et al.* (2009), which employs a locally adaptive coefficient C_1. It is also expected that the adaptive coefficients based on local flow features can partly compensate for the errors arising from the weak-equilibrium assumption by capturing some neglected advection and diffusion effects in the Reynolds stress anisotropy. An example is the correction proposed by Wallin & Johansson (2000) that adjusts the model coefficient C_1 in regions with low $\mathcal{P}/\varepsilon$, as provided in Appendix A.

The DES constant C_{DES} is also not universal. Different values have been used in various versions of DES models, e.g. 0.65 for Spalart–Allmaras-based DDES (Spalart *et al.* 2006), 0.78 and 0.61 for $k-\omega$ shear stress transport (SST)-based DDES (Gritskevich *et al.* 2012), and 0.12 for $\ell^2-\omega$ DDES (Reddy *et al.* 2014). Particularly, Yin *et al.* (2015) proposed a

https://doi.org/10.1017/jfm.2025.11022 Published online by Cambridge University Press

dynamic version for C_{DES}, which exhibits superior performance in various cases, and is necessary for a correct model behaviour in a transitional flow (Yin *et al.* 2021). Given these findings, the present study aims to offer a data-driven DES method to construct the adaptive model coefficients C_1, C_2, and C_{DES} based on local flow features.

3.1. *Neural network-based representation of model coefficients*

The present work employs a fully connected neural network to represent the mapping from local field variables to the model coefficients. Selecting appropriate input features is crucial for obtaining an accurate and generalizable model. Various features have been used in data-driven turbulence models (Duraisamy 2021). In the present work, the five invariants θ_i (as defined in (2.10)) are used as input features for the neural network. This is in light of the fact that the tensor basis coefficients β_i can generally be expressed as functions of these invariants (Pope 1975). Moreover, the same features have been used in the neural network-based closure of the Reynolds stress (Ling, Kurzawski & Templeton 2016) and subgrid stress (Bose & Roy 2024).

The input features are scaled into the range of $[-1, 1]$ by $\theta_i^* = \theta_i/(|\theta_i| + 1)$ to facilitate the training convergence. This approach falls into the category of input normalization based on local quantities, $\theta_i^* = \hat{\theta}_i/(|\hat{\theta}_i| + \theta_0)$, where $\hat{\theta}$ is the dimensional scalar invariants, calculated from the dimensional strain and rotation rates, and θ_0 is the local normalization factor defined from the turbulent time scale $1/(C_\mu\omega)$. This has been widely adopted in data-driven turbulence modelling (Wang, Wu & Xiao 2017; Wu, Xiao & Paterson 2018). In the present study, the dimensional scalar invariants $\hat{\theta}_i$ are normalized based on $C_\mu\omega$ to obtain θ_i, leading to the equivalent expression of $\theta_i^* = \theta_i/(|\theta_i| + 1)$. This approach has been shown to yield satisfactory training performance (Ling & Templeton 2015; Wu *et al.* 2025).

Moreover, to improve numerical stability, the local coefficients C_1, C_2, and C_{DES} provided by the neural network are averaged over the face neighbour cells, weighted by the surface areas of the common faces. Such approaches have been employed in the practical implementation of the dynamic Smagorinsky model and the adaptive $\ell^2 - \omega$ DDES model (Yin *et al.* 2015) when determining a local dynamic model coefficient.

In this work, the architecture of the neural network includes two hidden layers with 10 neurons per layer, with the weight vector $\boldsymbol{w}$ having 203 components. The sensitivity of the architecture has been investigated in the previous study (Zhang *et al.* 2022), showing that the chosen network is adequate for providing converged model outputs. The rectified linear unit activation function is used for the hidden layers, and the linear activation function is used for the output layer. The open-source library TensorFlow (Abadi *et al.* 2016) is employed to construct the neural network.

The schematic of the present data-driven EAS-DDES method is illustrated in figure 1. Specifically, the governing equations of the flow quantities $\bar{\boldsymbol{u}}$, k and ω are solved in the DES solver. Then the tensor invariants θ_i and the tensor basis $\boldsymbol{T}_i$ are calculated. The invariants θ_i are fed into the neural network to obtain the model coefficients C_1, C_2 and C_{DES} as outputs. With C_1, C_2 and θ_j determined, the tensor basis coefficients β_i can be obtained. Further, the coefficients β_i and C_{DES} determine eddy viscosity ν_t through (2.4)–(2.7). Meanwhile, β_i and $\boldsymbol{T}_i$ determines the nonlinear extra anisotropy $\boldsymbol{a}^*$ as (2.8) and (2.9). Finally, the modelled stress $\boldsymbol{\tau}$ is constructed based on (2.3), which is incorporated with the DES solver for solving the governing equations. The present study employs the open-source finite-volume CFD toolbox – OpenFOAM (Jasak, Jemcov & Tukovic 2007) – as the simulation platform. The specific mapping from the input features (θ_i) to the output coefficients (C_1, C_2 and C_{DES}) for the neural network is determined by the parameter vector $\boldsymbol{w}$ (which consists of the weights and biases) of the neural network. The optimal $\boldsymbol{w}$ is obtained by ensemble Kalman-based training.

https://doi.org/10.1017/jfm.2025.11022 Published online by Cambridge University Press

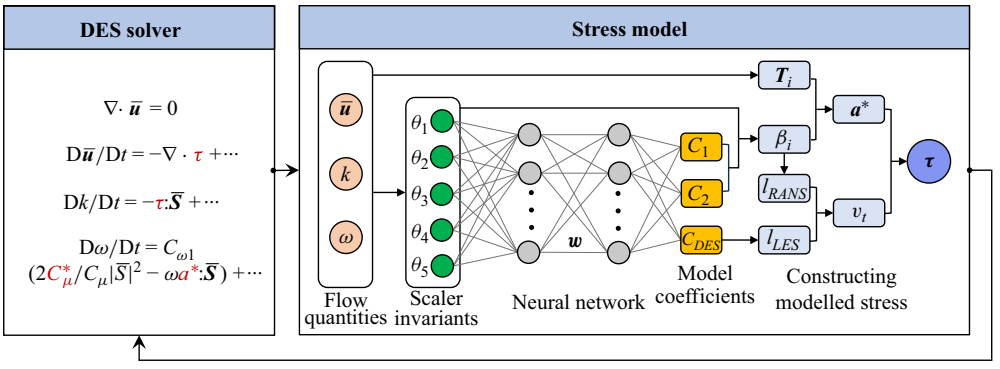


Figure 1. Schematic of the present data-driven EAS-DDES method with the model coefficients represented by neural networks.

3.2. *Ensemble Kalman method for training neural network-based model*

The objective of the model training in the present work amounts to finding the optimal neural network weights $\boldsymbol{w}$ that minimize the model prediction error. The iterative ensemble Kalman method with adaptive stepping (Zhang *et al.* 2022) is employed for training the weights $\boldsymbol{w}$, which is briefly introduced here.

In the ensemble-based approach, the corresponding cost function reads (Zhang, Michelén-Ströfer & Xiao 2020)

$$J=\left\|\boldsymbol{y}-\mathcal{H}(\boldsymbol{w}_j^l)\right\|^2_{\gamma\boldsymbol{R}}+\left\|\boldsymbol{w}_j^{l+1}-\boldsymbol{w}_j^l\right\|^2_{\boldsymbol{P}}, \tag{3.1}$$

where l is the iteration index, j is the sample index, $\|\cdot\|_{\boldsymbol{A}}$ indicates weighted norm (defined as $\|\boldsymbol{v}\|^2_{\boldsymbol{A}}=\boldsymbol{v}^T\boldsymbol{A}^{-1}\boldsymbol{v}$ for a vector $\boldsymbol{v}$ with weight matrix $\boldsymbol{A}$), $\boldsymbol{P}$ is the model error covariance matrix indicating the uncertainties of the initial parameters, $\boldsymbol{R}$ is the data error covariance matrix, γ is a scaling parameter for an adaptive adjustment of the step size at each iteration and $\boldsymbol{y}$ is the training data subjected to the Gaussian noise $\epsilon\sim\mathcal{N}(0,\,R)$. For convenience, the operator $\mathcal{H}$ denotes a composition of the DES solver and the associated postprocessing, which maps the weight parameters $\boldsymbol{w}$ to the observed quantities (e.g. mean velocity). In (3.1), the first term represents the discrepancy between the model prediction and the training data. The second term is the regularization term, which penalizes large variation of $\boldsymbol{w}$ from the last iterative step.

By minimizing the cost function, the update scheme of the iterative ensemble Kalman method can be derived as

$$\boldsymbol{w}_j^{l+1}=\boldsymbol{w}_j^l+\boldsymbol{K}^l\left[\boldsymbol{y}-\mathcal{H}(\boldsymbol{w}_j^l)\right], \tag{3.2}$$

with $\boldsymbol{K}^l$ being the Kalman gain matrix calculated as

$$\boldsymbol{K}^l=\boldsymbol{S}_w^l(\boldsymbol{S}_y^l)^T\left[\boldsymbol{S}_y(\boldsymbol{S}_y)^T+\gamma^l\boldsymbol{R}\right]^{-1}. \tag{3.3}$$

The square-root matrices $\boldsymbol{S}_w^l$ and $\boldsymbol{S}_y^l$ at each iteration are defined as

$$\begin{aligned}\boldsymbol{S}_w^l&=\frac{1}{\sqrt{N_j-1}}\left[\boldsymbol{w}_1^l-\hat{\boldsymbol{w}}^l,\,\boldsymbol{w}_2^l-\hat{\boldsymbol{w}}^l,\,\ldots,\,\boldsymbol{w}_{N_j}^l-\hat{\boldsymbol{w}}^l\right],\\ \boldsymbol{S}_y^l&=\frac{1}{\sqrt{N_j-1}}\left[\mathcal{H}_1^l-\hat{\mathcal{H}}^l,\,\mathcal{H}_2^l-\hat{\mathcal{H}}^l,\,\ldots,\,\mathcal{H}_{N_j}^l-\hat{\mathcal{H}}^l\right],\end{aligned} \tag{3.4}$$

https://doi.org/10.1017/jfm.2025.11022 Published online by Cambridge University Press

where N_j is the sample size, and $\hat{\boldsymbol{v}}$ denotes the averaging of a vector $\boldsymbol{v}$ in the sample space. The parameter γ^l is adjusted in an inner loop (Zhang *et al.* 2022).

As emphasized in § 1, it is crucial to ensure a reasonable RANS/LES switching behaviour for a data-driven DES model. For the present DD-EAS-DDES approach, the switching behaviour is mainly controlled by C_{DES} and C_μ^*, where C_μ^* is a function of tensor coefficients β_i and the invariants θ_j as (2.12). Here β_i are explicitly solved from the algebraic (2.19) of modelled stress anisotropy with the model coefficients C_1 and C_2 determined. Given that C_μ^* directly controls the RANS length scale and C_{DES} determines the LES length scale, their relative magnitude imposes direct influence on the RANS-to-LES switching. Thus, the trained C_1, C_2 and C_{DES} are not allowed to deviate far away from baseline values, thereby maintaining a similar switching behaviour as the baseline EAS-DDES model. Hence, besides the flow quantities q (e.g. mean velocity), the coefficients C_1, C_2 and C_{DES} normalized by the baseline values are also treated as the model outputs, with the ones viewed as the reference data, i.e.

$$\begin{aligned} \boldsymbol{y} &= \left[\alpha\frac{\langle q\rangle_{data}}{q_{ref}},\ 1,\ 1,\ 1\right], \\ \mathcal{H}\left(\boldsymbol{w}_j^l\right) &= \left[\alpha\frac{\langle q\rangle_{DES}}{q_{ref}},\ \frac{\langle C_1\rangle}{1.8},\ \frac{\langle C_2\rangle}{5/9},\ \frac{\langle C_{DES}\rangle}{0.12}\right], \end{aligned} \tag{3.5}$$

where q_{ref} is the reference value of q (e.g. q_{ref} is the bulk or free stream velocities when q represents the mean velocity), and α is the weight between the flow quantities and the model coefficients. Here a large value of $\alpha = 100$ is set to ensure the dominant role of $\langle u\rangle$ in the training process. It has been verified that using values of $\alpha = 50$ or 200 leads to negligible differences in the training results. This augmented observation is equivalent to adding a regularization term based on C_1, C_2 and C_{DES} in the cost function (Zhang *et al.* 2021).

Another benefit of treating the model coefficients as the training data is the ease of bounding their values to remain within physically meaningful ranges. Specifically, C_{DES} is supposed to be non-negative for the physical subgrid viscosity, and C_1 is required to be greater than unity for an 'return to isotropy' behaviour of $\boldsymbol{a}$ (Pope 2000). Without the constraints on the model coefficients, these criteria can be violated during the training process.

The training algorithm involves the following steps.

(i) Pretraining. The neural network weight vector $\boldsymbol{w}$ is pretrained as $\boldsymbol{w}^{\boldsymbol{0}}$ to perform as the baseline EAS-DDES model, i.e. $C_1 = 1.8$, $C_2 = 5/9$, $C_{DES} = 0.12$. This can facilitate the training convergence and avoid non-physical coefficients when using conventional weight initialization methods.

(ii) Sampling. Samples of the weight $\boldsymbol{w}$ are drawn from the normal distribution $\mathcal{N}(\boldsymbol{w}^{\boldsymbol{0}}, \sigma^2)$. Each realization $\boldsymbol{w}_j$ represents a specific neural-network-based turbulence model.

(iii) Propagation. Each sample of $\boldsymbol{w}$ provides a specific mapping from the scalar invariants θ_i to the model coefficients C_1, C_2 and C_{DES}. As such, the turbulent stress is closed, and the DES solver is executed to acquire the statistics of the flow field, as described in § 3.1. The model predictions in the observation space $\mathcal{H}_j^l$ are further obtained via postprocessing (e.g. extracting mean velocities at specific points).

(iv) Kalman update. With the predictions $\mathcal{H}_j^l$ and the corresponding training data $\boldsymbol{y}$, the weight vector $\boldsymbol{w}_j^l$ can be updated using the ensemble Kalman method described above.

https://doi.org/10.1017/jfm.2025.11022 Published online by Cambridge University Press

Steps (iii) and (iv) are repeated until one of the samples $\boldsymbol{w}_j^l$ reaches the convergence criteria. This sample of neural network weights is employed as the trained model in this work. For details of the ensemble Kalman method and its practical implementation in turbulence modelling, please refer to Zhang *et al.* (2022). In the present work, the DAFI code (Michelén-Ströfer *et al.* 2021) is used to implement the aforementioned training algorithm.

4. Secondary flow in a square duct

The proposed data-driven DES method is first tested for secondary flows in a square duct. Explicit algebraic stress-based models offer a key advantage over LEV models by capturing Reynolds stress anisotropies, which are essential for representing turbulent secondary motions. The square duct flow is one of the canonical secondary flows for testing the predictive performance of turbulence models. The cross-stream secondary flow in a square duct is driven by the normal stress anisotropy $\tau_{yy} \neq \tau_{zz}$ and the shear stress τ_{yz} (Pettersson Reif & Andersson 2002; Durbin 2011). Hence, we assess the ability of the proposed method in learning algebraic stress-based DES models for the secondary flow in a square duct. The baseline EAS-DDES model (Liu *et al.* 2024*b*) has been used to simulate a square duct flow with bulk Reynolds number $Re_b = 2\delta u_b/\nu = 40\,000$, where δ is the duct half-side, and u_b is the bulk velocity. The prediction is compared with the DNS result (Pirozzoli *et al.* 2018), showing substantially better accuracy than traditional LEV-DDES models, e.g. the $\ell^2 - \omega$ DDES (Reddy *et al.* 2014) and the IDDES-SST (Gritskevich *et al.* 2012) models. Here we show that the proposed method can further improve the predictive accuracy by providing the neural network-based model coefficient closures.

4.1. *Case set-up and numerical methods*

The square duct flow with $Re_b = 17\,800$ is chosen to train the model based on the DNS data of Pirozzoli *et al.* (2018). The computational domain length is $L_x = 20\delta$ in the streamwise direction. The structural mesh consists of 1.024×10^6 cells, with 160 cells in the streamwise direction and 80 cells in the duct side direction. The grid is uniformly distributed in the streamwise direction, with the mean wall-unit normalized size $\Delta x^+ \approx 30$. The grid spacing is progressively refined in the wall-normal direction, with the cell size of the near-wall first layer being $\Delta y_1^+ < 1$. The maximum cell spacing in cross-stream directions is $\Delta y_{max}^+ = \Delta z_{max}^+ \approx 15$. The streamwise boundaries are set as periodic, and the other boundaries are no-slip walls. A global pressure gradient drives the flow to maintain a desired value of Re_b.

The flow statistics are obtained by averaging over time, the homogeneous streamwise direction, and the four quadrants. Due to the weakness of the secondary flow, the required averaging time interval Δt_{av} to achieve statistical convergence is extremely long. To account for the influence of streamwise extent of the domain in the statistical convergence (Pirozzoli *et al.* 2018), the effective time averaging intervals are set as $\Delta t_{av}^* = \Delta t_{av} L_x/(6\delta) \approx 200\delta/u_\tau$ to achieve the statistical convergence of the first-order moment of the velocity field during the training process.

The numerical scheme achieves second-order accuracy in both time and space. The central linear scheme is utilized for momentum convection. For the convection of turbulence variables, i.e. k and ω, the central linear scheme with the Sweby limiter is applied to ensure boundedness. Diffusion terms are treated using central linear interpolation for face values and Gauss's theorem for surface integrals. Time discretization is performed using the second-order implicit Euler method. The time step size is

https://doi.org/10.1017/jfm.2025.11022 Published online by Cambridge University Press

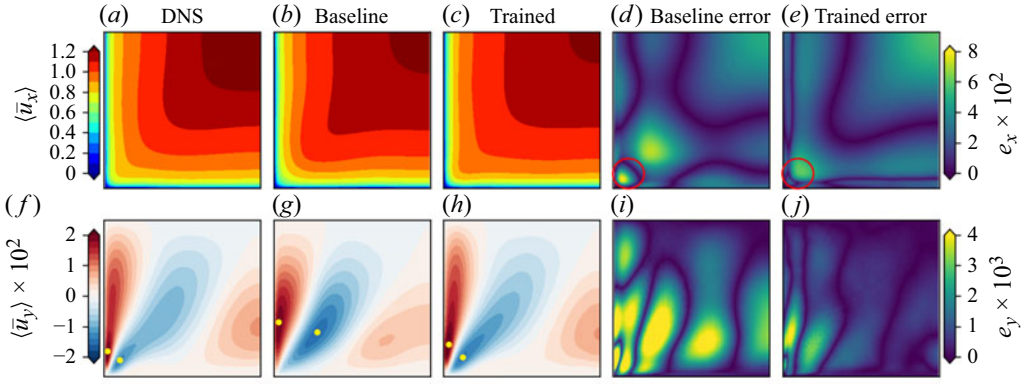


Figure 2. Mean velocity in (*a–c*) x- and (*f–h*) y-directions and absolute prediction error contours in (*d*,*e*) x- and (*i*,*j*) y-directions in the third quadrant ($y < 0$, $z < 0$) for the square duct.

dynamically adjusted to maintain the maximum Courant–Friedrichs–Lewy number below 0.5. The coupling between pressure and velocity is managed through the PIMPLE algorithm. A preconditioned conjugate gradient solver is employed for the pressure equation, while other transport equations are solved using a preconditioned biconjugate gradient method.

The training data set consists of the mean velocities $\langle \bar{u}_x \rangle$, $\langle \bar{u}_y \rangle$ and $\langle \bar{u}_z \rangle$ in the whole computational domain, with $\langle \bar{u}_y \rangle$ and $\langle \bar{u}_z \rangle$ being scaled up by a factor of 50 to have a similar maximum magnitude with $\langle \bar{u}_x \rangle$. The training data is weighted by the local cell volume. During model training with the ensemble Kalman method, 16 samples are drawn in this case, and convergence of the cost function is achieved within approximately five iterative steps. In each iteration step, the computational cost for each sample is approximately 1000 central processing unit (CPU) hr (equivalent to the computational cost of the baseline or trained DD-EAS-DDES models in this case), resulting in a total training cost of 80 000 CPU hr.

4.2. *Prediction of velocity and modelled stress*

The mean velocity contours predicted by the baseline and trained EAS-DDES models are compared with the DNS results in figure 2(*a–c*,*f–h*). Only the third quadrant is shown due to the flow symmetry. The accuracy of the trained model outperforms the baseline model in both the main flow ($\langle \bar{u}_x \rangle$) and the secondary flow ($\langle \bar{u}_y \rangle$). Figure 2(*d*,*e*,*i*,*j*) shows the absolute error of the predictions by both models with respect to the DNS data, defined as

$$e_{x,y} = \left| \left\langle \bar{u}_{x,y}^{trained} \right\rangle - \left\langle \bar{u}_{x,y}^{data} \right\rangle \right|. \tag{4.1}$$

The absolute error of the trained model is significantly reduced compared with the baseline model. For the streamwise mean velocity, the improvement of the trained model is significant near the corner of the duct, as marked by the red circles in figure 2(*d*,*e*). For the prediction of the secondary flow, the trained model performs remarkably better in the entire domain. It is observed that the peaks of cross-stream velocity (including both positive and negative values) predicted by the trained model are located near the corner regions in closer agreement with the DNS data compared with the baseline model, as marked by the yellow symbols in figure 2(*f–h*).

Figure 3(*a*,*b*) presents the mean velocity profiles at different cross-stream locations. It can be observed that there exist negligible differences in the streamwise mean velocity between the DNS results and the predictions by different models. For the secondary flow

https://doi.org/10.1017/jfm.2025.11022 Published online by Cambridge University Press

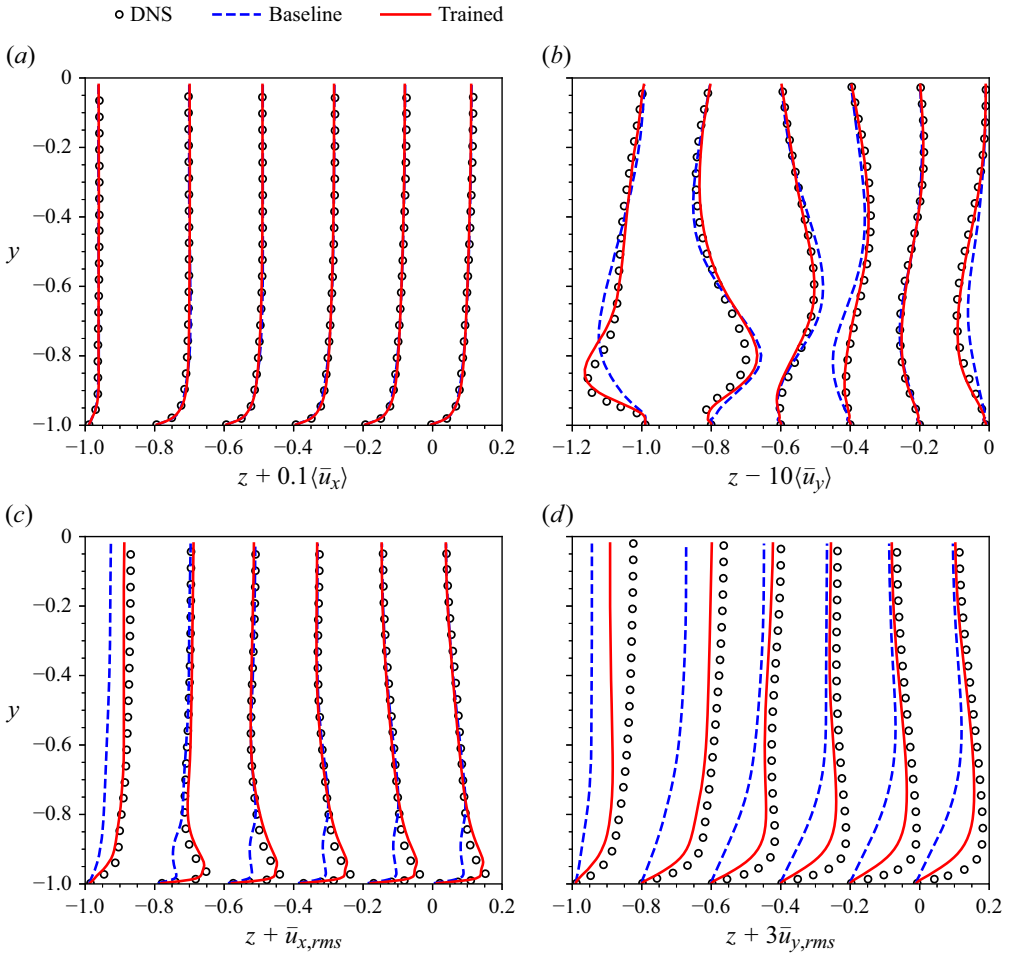


Figure 3. Comparison of the mean and r.m.s. velocity profiles between the DNS, the baseline EAS-DDES model and the trained DD-EAS-DDES model at $z = -0.99, -0.8, -0.6, -0.4, -0.2, 0$ for flows in the square duct.

predictions, a substantial improvement in prediction accuracy is observed for the trained model compared with the baseline model, especially in the near-wall region, e.g. $z = 0.99$. This indicates that the trained DES model is effective in both the RANS and the LES branches in this case.

As for the root-mean-square (r.m.s.) velocity profiles illustrated in figure 3(*c*,*d*), the trained model provides significantly better predictions than the baseline model in both the streamwise and the cross-stream directions. Overall, the baseline model under-predicts the r.m.s. velocities in the near-wall regions, while the trained model largely compensates for this due to the enlarged LES region. This will be further demonstrated in § 4.3.

To clarify the underlying mechanism of the improved velocity predictions, the normalized total stress $\hat{\boldsymbol{\tau}}/u_\tau^2$ is illustrated in figure 4, where u_τ is the wall-friction velocity from the DNS. For the DES, $\hat{\boldsymbol{\tau}}$ is defined as the summation of the resolved and the modelled parts as

$$\hat{\boldsymbol{\tau}} \equiv \langle \boldsymbol{u}'\boldsymbol{u}' \rangle = \langle \bar{\boldsymbol{u}}'\bar{\boldsymbol{u}}' \rangle + \langle \boldsymbol{\tau} \rangle. \tag{4.2}$$

https://doi.org/10.1017/jfm.2025.11022 Published online by Cambridge University Press

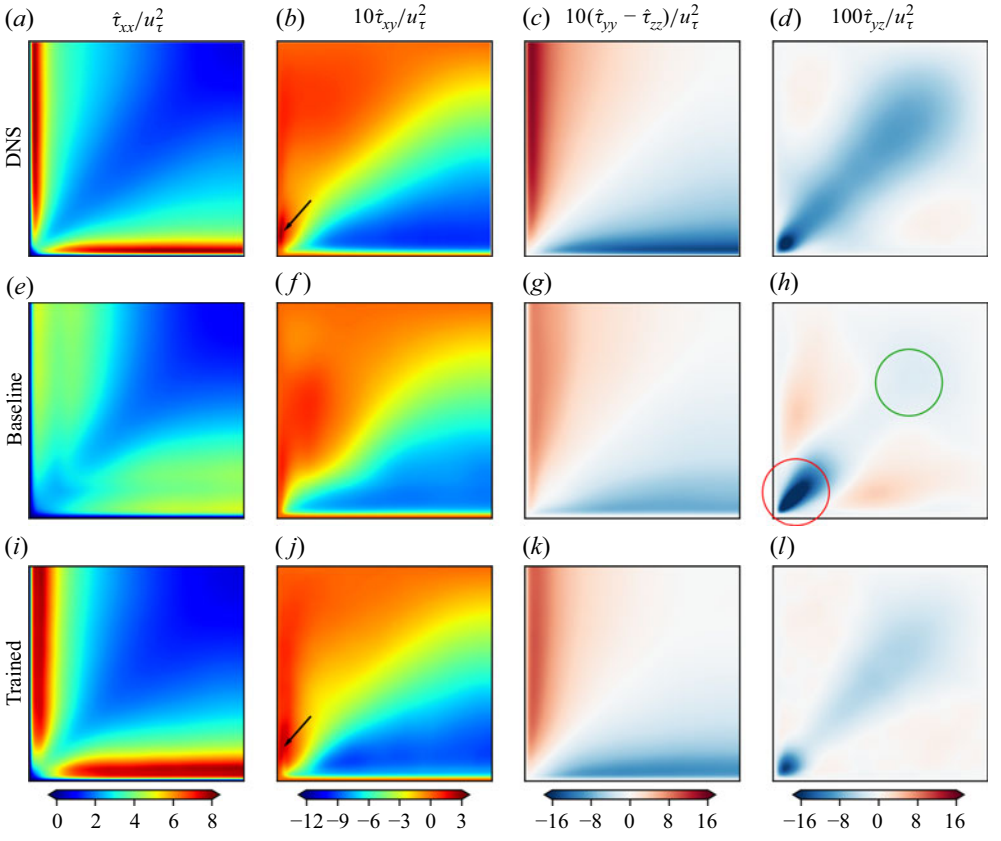


Figure 4. Comparisons of the normalized total stress between the (*a–d*) DNS, (*e–h*) the baseline EAS-DDES model and (*i–l*) the trained DD-EAS-DDES model in the third quadrant ($y < 0$, $z < 0$) of the square duct.

For the streamwise normal stress $\hat{\tau}_{xx}$, the baseline model underestimates the peak value and overestimates the thickness of the high $\hat{\tau}_{xx}$ region, while the prediction of the trained model is in better agreement with the DNS results. Similarly, for the streamwise shear stress $\hat{\tau}_{xy}$, the trained model provides better agreement with the DNS than the baseline model. Notably, the trained model reproduces the small positive peak near the corner observed in the DNS, as marked by the black arrows in figure 4(*b*,*j*), while the baseline model fails to capture it.

The inherent nature of the secondary flow can be illustrated by the mean streamwise vorticity equation

$$\left(\langle u_y\rangle\frac{\partial}{\partial y}+\langle u_z\rangle\frac{\partial}{\partial z}\right)\langle\omega_x\rangle-\nu\left(\frac{\partial^2}{\partial y^2}+\frac{\partial^2}{\partial z^2}\right)\langle\omega_x\rangle=\left(\frac{\partial^2}{\partial z^2}-\frac{\partial^2}{\partial y^2}\right)\hat{\tau}_{yz}+\frac{\partial^2}{\partial y\partial z}\left(\hat{\tau}_{yy}-\hat{\tau}_{zz}\right). \tag{4.3}$$

The four terms in (4.3) represent the effects of convection, diffusion, secondary turbulent shear stress and the turbulent normal stress anisotropy, respectively. The normal stress anisotropy ($\hat{\tau}_{yy}-\hat{\tau}_{zz}$) has been widely recognized as driving the streamwise vorticity due to its dominant magnitude. On the other hand, it is evident from numerical simulations (Pirozzoli *et al.* 2018) that the secondary turbulent shear stress term in the mean

https://doi.org/10.1017/jfm.2025.11022 Published online by Cambridge University Press

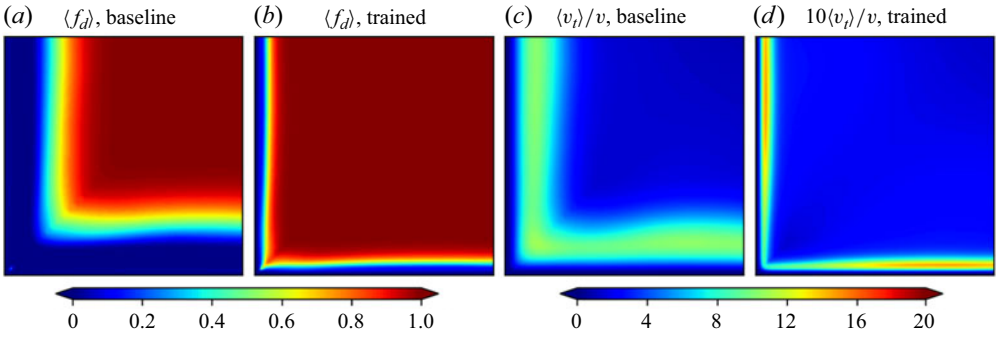


Figure 5. Comparisons of the shielding function f_d and the turbulent viscosity ratio ν_t/ν between the baseline EAS-DDES model and the trained DD-EAS-DDES model.

streamwise vorticity equation has a similar magnitude to the normal stress anisotropy term. Moreover, it is found that non-zero turbulence production is mainly associated with significant secondary shear stress. Given this, we plot both the normal stress anisotropy $(\hat{\tau}_{yy} - \hat{\tau}_{zz})$ and the secondary turbulent shear stress $\hat{\tau}_{yz}$, as shown in figure 4(*c*,*g*,*k*) and figure 4(*d*,*h*,*l*). The difference between the baseline and trained model predictions in $(\hat{\tau}_{yy} - \hat{\tau}_{zz})$ is marginal, with the predictions by the trained model in slightly better agreement with the DNS result. As for $\hat{\tau}_{yz}$, it is obvious that the trained model outperforms the baseline model. Specifically, the distribution of $\hat{\tau}_{yz}$ for the trained model prediction is similar to the DNS results. However, the baseline model significantly overestimates the magnitude of $\hat{\tau}_{yz}$ in the corner region (red circle), and underestimates it in the central region of the duct (green circle). These improvements in modelled stress lead to better velocity predictions of the secondary flow with the trained model than the baseline model.

4.3. *Switching behaviours and model coefficients*

Figure 5 compares the switching behaviours between the RANS and LES branches for the baseline and the trained models. Specifically, the mean shielding function $\langle f_d \rangle$ is shown in figure 5(*a*,*b*), and the mean eddy viscosity ratio $\langle \nu_t \rangle/\nu$ is shown in figure 5(*c*,*d*). Strictly speaking, the shielding function $\langle f_d \rangle$ in DDES ensures a shielded near-wall RANS region to prevent the GIS issue. Outside the shielded region, the RANS and LES length scales (ℓ_{RANS} and ℓ_{LES}) are compared locally to determine the RANS/LES mode, as described in § 2.2. Usually, $f_d = 1$ alone does not sufficiently indicate a LES region. However, in the present square duct flow simulations, the mesh is sufficiently fine outside the shielded region ($\Delta x^+ \approx 30$ and $\Delta y^+_{max} = \Delta z^+_{max} \approx 15$), ensuring $\ell_{LES} < \ell_{RANS}$ in these regions. Therefore, f_d is sufficient to indicate the switching behaviour in this case.

It can be seen that the trained model performs a much larger region of the LES branch as indicated with $\langle f_d \rangle = 1$. The near-wall RANS region is much thinner than that of the baseline model. This leads to a relatively small eddy viscosity ratio for the trained model, compared with the baseline. Note that $\langle \nu_t \rangle/\nu$ for the trained model in figure 5(*d*) is scaled by a factor of 10 for clarity. These facts indicate that the trained model enhances performance by enlarging the LES region to resolve more turbulent structures.

To explore the underlying reasons for the trained model's behaviour, the model coefficients C_1, C_2 and C_{DES}, and the calculated C^*_μ are examined. The relative variations of these model coefficients compared with the baseline values are presented in figure 6. As shown in figure 6(*d*), C^*_μ in the near-wall region is lower than the baseline value, which is determined by the variation of C_1 and C_2 from the baseline value. This coefficient

https://doi.org/10.1017/jfm.2025.11022 Published online by Cambridge University Press

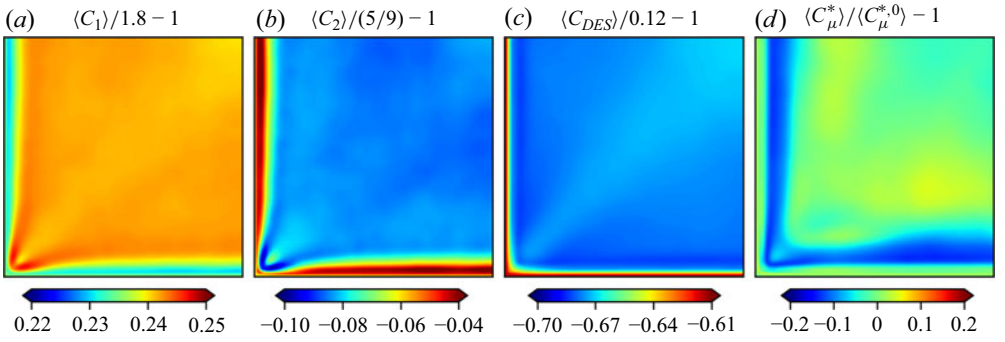


Figure 6. Mean values of the model coefficients $\langle C_1\rangle$, $\langle C_2\rangle$, $\langle C_{DES}\rangle$ and $\langle C_\mu^*\rangle$ of the trained DD-EAS-DDES model in the third quadrant ($y<0$, $z<0$) of the square duct. The coefficients are normalized by the baseline values.

directly controls f_d as (2.7). That is, a smaller C_μ^* leads to a larger value of f_d, consequently, a thinner shielded RANS region. Additionally, C_μ^* and C_{DES} jointly control the production term of the k transport equation as (2.1). The simultaneous decrease of C_μ^* and C_{DES} reduces the modelled kinetic energy, which further increases f_d. Therefore, both the variations of C_{DES} and C_μ^* result in enlarging the LES region and resolving more turbulent structures.

To investigate the effects of the trained model coefficients, we present the resolved and modelled parts of the turbulent stress as shown in figure 7. From figure 7(*a*,*b*,*e*,*f*), the increasing trend of resolved TKE portions for the trained model can be seen. For the baseline model, the modelled TKE is primarily distributed in the near-wall region, and the resolved part is distributed away from the wall, with both exhibiting a similar maximum magnitude. While for the trained model, TKE is almost fully resolved, with the modelled part being small.

As discussed above, the secondary flow is mainly driven by the turbulent normal stress anisotropy ($\hat{\tau}_{yy}-\hat{\tau}_{zz}$) and the secondary turbulent shear stress $\hat{\tau}_{yz}$. Specifically, the predictions of the baseline and the trained model have major differences in $\hat{\tau}_{yz}$ (see figure 4*d*,*h*,*l*). Figure 7(*c*,*d*,*g*,*h*) illustrate the resolved and modelled parts of $\hat{\tau}_{yz}$ for the baseline and trained models. For the baseline model, the modelled part accounts for a large proportion of $\hat{\tau}_{yz}$, while the resolved part is relatively small. The spatial distribution of τ_{yz} is very similar to the total one $\hat{\tau}_{yz}$ (figure 4*h*), and the deviation from the DNS result mainly comes from the modelling error. In contrast, the major contribution of $\hat{\tau}_{yz}$ is from the resolved part for the trained model, which is similar to the distribution of the DNS result (figure 4*d*). This further confirms that the better performance of the trained model is mainly attributed to the increase in the resolved turbulence.

The variations of the coefficients C_1 and C_2 have two main effects on the model prediction. The first is to alter the switching location between the RANS and LES regions by modifying C_μ^*. The second one is to alter the nonlinear extra anisotropy $\boldsymbol{a}^*$ by modifying the expressions of the tensor basis coefficients β_i as listed in the Appendix A. To assess the contribution of the second effect, a new simulation is conducted by using the baseline C_1, C_2 values, and the trained C_{DES} function. This can lead to a similar f_d distribution as the fully trained model, while the functions of β_i with respect to the scalar invariants θ_j are unchanged because of using the baseline C_1 and C_2 values. The results of the mean secondary velocity $\langle\bar{u}_y\rangle$ are shown in figure 8. Overall, the predictions from the partially trained case are similar to the fully trained case. A difference can be observed

https://doi.org/10.1017/jfm.2025.11022 Published online by Cambridge University Press

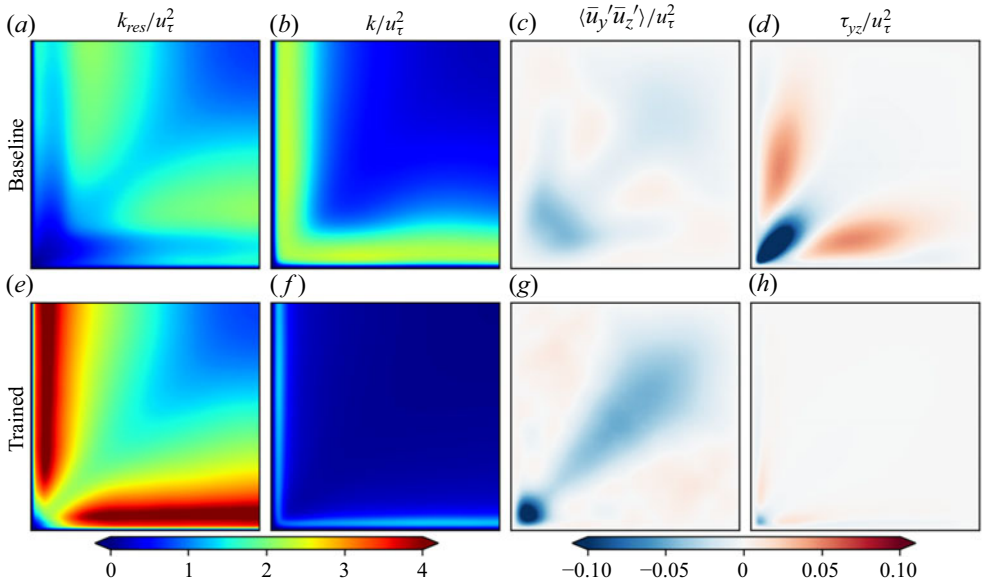


Figure 7. Comparisons of the mean resolved and modelled parts of TKE and secondary shear stress between the baseline EAS-DDES model and the trained DD-EAS-DDES model in the third quadrant ($y < 0$, $z < 0$) of the square duct.

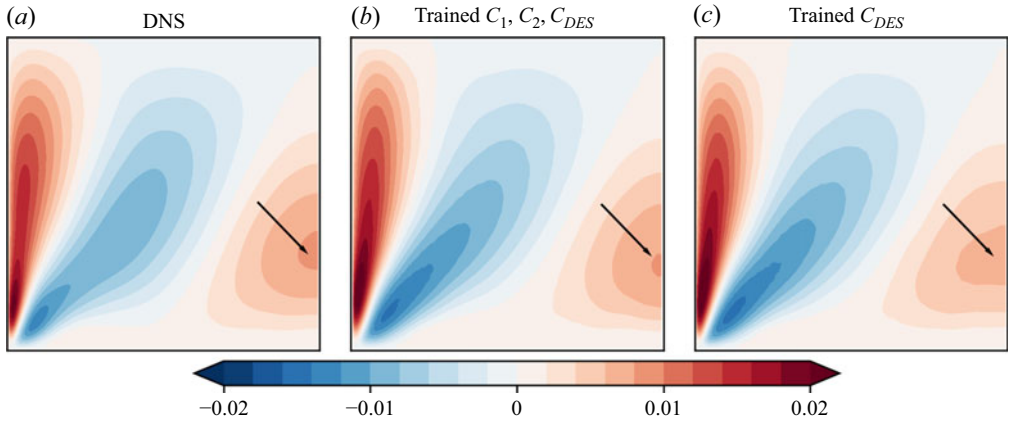


Figure 8. Comparison of the mean secondary velocity $\langle \bar{u}_y \rangle$ between the DNS, the fully trained DD-EAS-DDES model and the DD-EAS-DDES model with trained C_{DES} in the third quadrant ($y < 0$, $z < 0$) of the square duct.

in the positive $\langle \bar{u}_y \rangle$ region near the central line ($z = 0$), as pointed by the black arrows, where the fully trained model has slightly better performance than the partially trained one. Hence, the modifications of β_i functions with the trained C_1 and C_2 have positive effects on the model performance, although the impact is weaker than the modification of LES/RANS switching location via the trained C_{DES}.

4.4. *Generalization in Reynolds number*

The generalizability of the trained model is further assessed in two square duct flows of $Re_b = 7000$ and 40 000. The mesh is the same as the trained case, which means the grid

https://doi.org/10.1017/jfm.2025.11022 Published online by Cambridge University Press

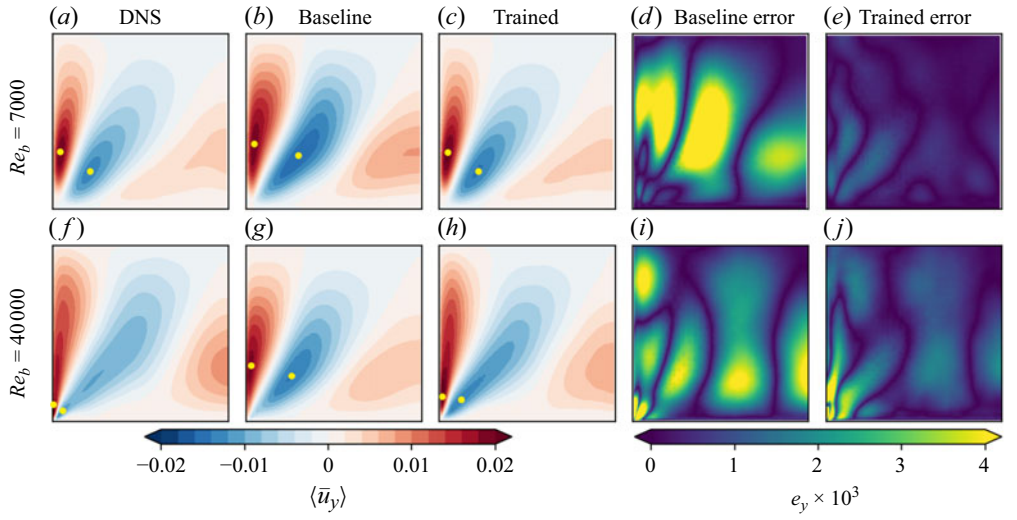


Figure 9. (*a–c*,*f–h*) The mean secondary velocity $\langle \bar{u}_y \rangle$ of the DNS result, the predictions by the baseline and trained EAS-DDES models and (*d*,*e*,*i*,*j*) the absolute errors for the baseline and trained models in the third quadrant ($y < 0$, $z < 0$) of the square duct flow with (*a–e*) $Re_b = 7000$ and (*f–j*) $Re_b = 40\,000$. The model is trained in the square duct flow with $Re = 17\,800$.

resolution relative to turbulence scales varies due to the variation of the Reynolds number, with a larger proportion of turbulent scales being modelled at a higher Reynolds number. As such, the model's generalizability can also be assessed in the grid resolution with respect to the turbulence scales. The secondary flow predictions of the baseline and the trained models are compared with the DNS result in figure 9. A significant improvement in the accuracy of the trained model is observed for both cases, which is similar to the case of $Re_b = 17\,800$ as shown in figure 2(*f–h*). The predicted locations of the positive and negative peaks of $\langle \bar{u}_y \rangle$ (as marked by the yellow symbols) are closer to the duct corner with the increase of Reynolds number, and the positive $\langle \bar{u}_y \rangle$ near the central line ($z = 0$) is better predicted than the baseline model. Compared with the baseline model, the trained model's absolute errors are remarkably reduced for both cases in the whole domain. Conclusively, the trained model can be well generalized to flows with this different Reynolds number.

The switching behaviours of the trained model can be well generalized to the cases with different Reynolds numbers. It is supported in figure 10, which compares the switching behaviours of the $Re_b = 7000$ and $Re_b = 40\,000$ cases. Both cases are simulated based on the DD-EAS-DDES model trained by the $Re_b = 17\,800$ case. The distribution of f_d is almost unchanged for the two different Reynolds numbers, while the eddy viscosity ratio $\langle \nu_t \rangle / \nu$ in the near-wall RANS region becomes significantly larger for higher Reynolds numbers. For clarity, $\langle \nu_t \rangle / \nu$ is scaled by a factor of 10 for the $Re_b = 7000$ case in figure 10(*c*). This indicates a larger proportion of modelled stress at higher Reynolds numbers.

5. Separated flows over a bump

We further test the proposed data-driven detached-eddy simulation method in the flow over a bump, which is another challenging case for either the RANS or DES models. Deck (2012) classifies the flow separation into three categories. The first one is the separation fixed by the geometry, such as the separated flow over a backward-facing step.

https://doi.org/10.1017/jfm.2025.11022 Published online by Cambridge University Press

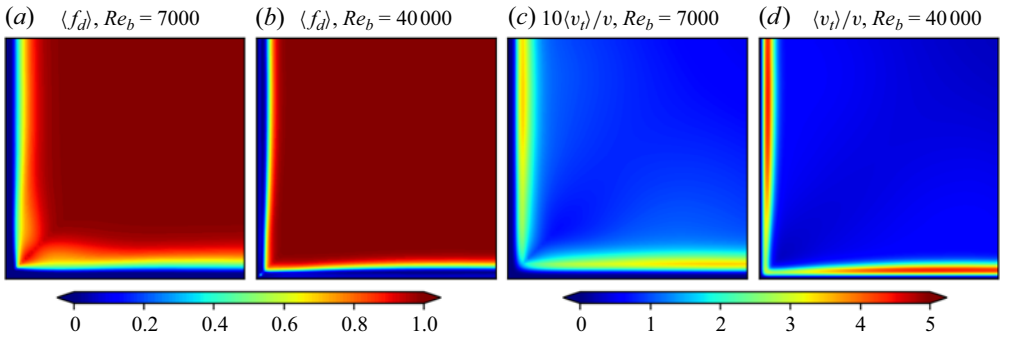


Figure 10. Comparisons of the time-averaged DDES shielding function f_d and the turbulent viscosity ratio ν_t/ν between the $Re_b = 7000$ and the $Re_b = 40\,000$ cases simulated by the trained DD-EAS-DDES model. The model is trained in the square duct flow with $Re = 17\,800$.

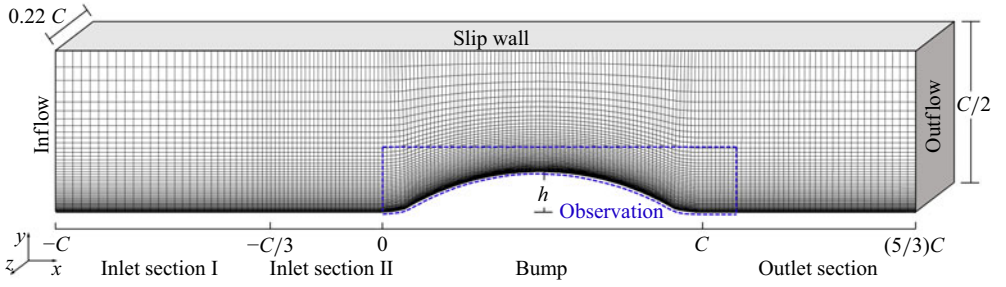


Figure 11. The computation domain and mesh on the x–y plane for the separated flow over a bump.

The second and third categories are the separation induced by a pressure gradient on a curved surface. The second one has an inflow boundary layer thickness $\delta/H \ll 1$, where H is the characteristic height of the curved surface, while the third one has $\delta/H = O(1)$. For the third category, the separation is strongly influenced by the dynamics of the incoming turbulent boundary layer. The turbulence statistics inside the boundary layer are strongly affected by the pressure gradient over the curved surface. The investigated flow over the bump belongs to the third category. The favourable pressure gradient (FPG) in the upstream side of the bump accelerates the mean flow while reducing the turbulent intensity, which may cause relaminarization (Balin & Jansen 2021). On the other hand, the adverse pressure gradient (APG) in the downstream side of the bump decelerates the mean flow, enhancing the turbulence and causing the flow separation. These features pose significant challenges for turbulence modelling of the flow over a bump, especially in capturing the separation point, the extent of the separated region and the subsequent reattachment behaviour accurately (Durbin 2018). The wall-resolved LES (WRLES) datasets by Matai & Durbin (2019*b*) are used to evaluate the capability of the DD-EAS-DDES model in such flows. In the datasets, the LES results of flow over a parametric set of bumps with different crest heights are available, which are used for the generalization test of data-driven DES models.

5.1. *Case set-up and numerical methods*

The flow over the bump with $h = 38$ mm is chosen to train the DES model. The computational domain and mesh on the xy plane are shown in figure 11. The length of the bump is $C = 305$ mm, which consists of a circular arc with a chord length of $(5/6)C$

https://doi.org/10.1017/jfm.2025.11022 Published online by Cambridge University Press

and convex fillets with a radius of $0.323C$ added before and after the arc. The Reynolds number of the bump case is $Re_c = 2 \times 10^5$ based on the free stream velocity and the bump length. Before the bump, the inlet section consists of two parts. The inlet section I with a length of $(2/3)C$ is added to ensure adequate development of synthetic turbulence introduced at the inlet. The inlet section II has a length of $C/3$, which is consistent with the LES configuration. The outlet section length after the bump is $(2/3)C$. The height of the domain is $C/2$, and the width is $0.22C$. The computational domain is the same as the LES case (Matai & Durbin 2019*b*) except for the inclusion of the inlet section I.

The structural mesh consists of 0.42×10^6 cells, with 175, 60 and 40 cells in the streamwise, wall-normal and spanwise directions, respectively. In the streamwise direction, the grid is uniformly distributed for inlet section I and the bump region, with the cell size $\Delta x/C = 0.013$ and $\Delta x^+ \approx 100$. For the inlet section II and the outlet section, the grid size is stretched in the streamwise direction by a factor of two towards the inlet and the outlet, respectively. In the wall-normal direction, the grid spacing is progressively refined towards the bottom wall, with the cell size of the near-wall first layer satisfying $\Delta y_1^+ < 1$. The grid is uniformly distributed in the spanwise direction, with the normalized size $\Delta z/C = 0.0055$ and $\Delta z^+ \approx 40$.

The periodic boundaries are set for the spanwise direction. The slip and no-slip boundaries are set for the top and bottom walls, respectively. The outlet is imposed with fixed pressure, zero velocity gradient and non-reverse flow. At the inlet, the velocity follows LES practice by adding synthetic turbulence to the mean velocity profile to obtain the instantaneous velocity. The synthetic turbulence is constructed by the synthetic digital filter method (Klein, Sadiki & Janicka 2003). It employs the digital filtering of random data to reproduce specified second-order (single-point) statistics and the autocorrelation functions of the velocity. The synthetic digital filter method has been widely used in generating desired inflow turbulence in eddy-resolving simulations (Wu 2017). The required mean velocity, Reynolds stress and integral length profiles are provided by a precursor RANS simulation of a zero-pressure-gradient flat plate. The streamwise location x_0 with the same boundary layer thickness as the LES inlet is prescribed, and the profiles at $x = x_0 - (2/3)C$ are extracted for generating the inlet instantaneous velocity. For the turbulence properties, the ω profile is also extracted from the precursor RANS simulation of the flat plate. In the DES, k represents the modelled part of TKE, which is set to zero at the inlet, and synthetic turbulence is introduced to represent the resolved TKE. The subgrid TKE is underestimated near the inlet, while it can be developed to a physical value after the inlet section I.

The numerical schemes are the same as the square duct flow case described in § 4.1. The time step size is fixed at a value with a maximum Courant–Friedrichs–Lewy number of approximately 0.5. The flow statistics are obtained by averaging over time and spanwise direction, with the averaging time interval $\Delta t_{av} \approx 8C/u_b$.

In this case, the flow separation and reattachment are of primary interest. Given this, the training data are selected between the beginning of the bump ($x/C = 0$) and the reattachment point ($x/C = 1.1$) based on the LES in the x direction. The range in the y direction is $y < 0.2C$. The observation region is shown as the blue dashed lines in figure 11. In this region, flow data are extracted along 23 parallel vertical lines with an interval of $0.05C$ in the x direction. For all cells along these lines, the mean streamwise velocity divided by the local wall distance, $\langle \bar{u}_x \rangle / d_w$, is used as the training data. Here, d_w is introduced to compensate for the small velocity values near the wall, as suggested by Matai & Durbin (2019*b*). The training data is also weighted by the local cell volume. As for the ensemble Kalman method, 16 samples are drawn in this case, which is the same as the square duct case. The convergence is achieved in approximately 20 iterative steps.

https://doi.org/10.1017/jfm.2025.11022 Published online by Cambridge University Press

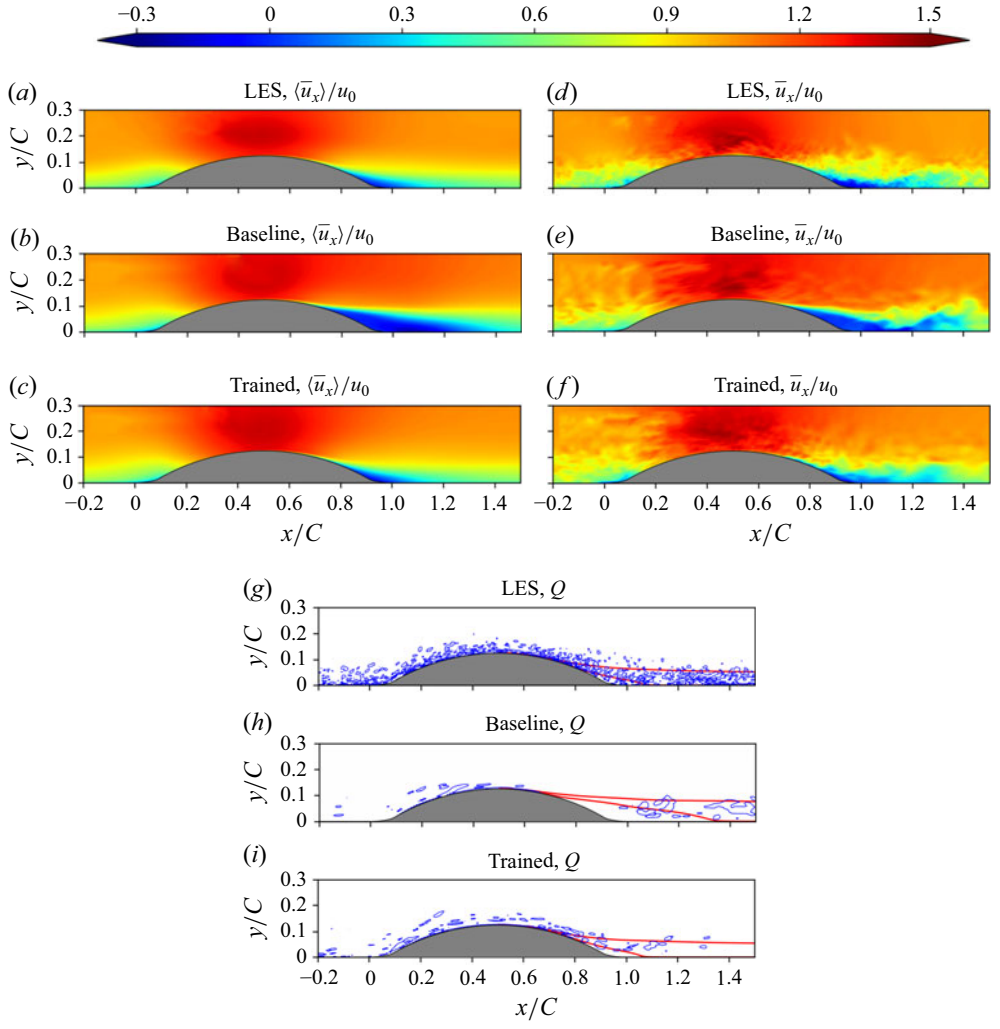


Figure 12. Comparisons of the normalized instantaneous and mean streamwise velocity contours and the Q-criteria contours at $Q = 2 \times 10^5\ \mathrm{s}^{-2}$, between the ($a$,$d$) LES, ($b$,$e$) baseline EAS-DDES model and (c,f) trained DD-EAS-DDES model for flows over the bump.

In each training step, the computational cost for each sample is approximately 50 hr of CPU time (equivalent to the computational cost of the baseline or trained DD-EAS-DDES models in this case), resulting in a total training cost of 16 000 CPU hr.

5.2. *Predictions of velocity and skin friction coefficient*

Figure 12(a–c) shows the normalized mean streamwise velocity contours. Both the baseline and trained models are in good agreement with the LES data upstream of the bump crest, where the flow experiences a weak APG to FPG. However, in the region of strong APG after the bump crest, a substantial difference is observed in the predictions by both models. Compared with the LES result, the baseline EAS-DDES model predicts the separation point too early, leading to a significantly large recirculation zone. In contrast, the prediction of the trained model is in excellent agreement with the LES result. Both the separation and reattachment locations are accurately predicted.

https://doi.org/10.1017/jfm.2025.11022 Published online by Cambridge University Press

Regarding the instantaneous streamwise velocity, as shown in figure 12(*d–f*), both the baseline and the trained models resolve the turbulent motions well before the bump crest. The main difference in the instantaneous velocity fields between the two models is located in the separated shear layer after the bump crest. The prediction of the baseline model exhibits a strong delay of transition from modelled to resolved turbulence in the separated shear layer, known as the 'grey area' issue in hybrid RANS-LES approaches (Probst *et al.* 2017; Pont-Vílchez *et al.* 2021; Wang, Tang & Liu 2025). In contrast, the trained model exhibits a reasonable development of the resolved turbulent motions in the shear layer. The resolved turbulent motions occur much earlier than the baseline model and are consistent with the LES results.

The comparison is also made in the instantaneous contour lines of Q-criterion, as depicted in figure 12(*g–i*). The blue lines denote $Q = 2 \times 10^5\ \mathrm{s}^{-2}$, and the red lines mark $\langle \bar{u}_x \rangle / u_0 = 0.2, 0.8$ after the bump crest to indicate the separated shear layer. Both models predict larger turbulent structures than the LES due to the coarser mesh. With the trained model, the predicted turbulent motions occur immediately upon shear layer separation, which agrees with the LES result. In contrast, the baseline model suffers from the 'grey area' issue, predicting a strong delay in the occurrence of turbulent motions in the separated shear layer.

Figure 13(*a*,*b*) shows the mean velocity profiles in the streamwise and wall-normal directions. Before the bump crest, both models can predict the velocity profiles well. However, the baseline model exhibits large discrepancies from the LES after the bump crest due to the incorrect predictions of the separation and reattachment points. In contrast, the predictions of the trained model agree well with the LES results. Although only the streamwise mean velocity is used in the loss function during the training process, the wall-normal velocity is also accurately predicted by the trained model. This can be explained by the divergence-free constraint of the mean flow. That is, the accurate prediction of $\langle \bar{u}_x \rangle$ inherently improves the prediction of $\langle \bar{u}_y \rangle$ in this spanwise-homogeneous case with $\bar{u}_z = 0$.

The r.m.s. velocity profiles are also significantly better predicted with the trained model than the baseline model, as shown in figure 13(*c*,*d*). At $x/C = 0.8$, the baseline model under-predicts the velocity fluctuations due to the delayed unsteadiness in the separated shear layer, as illustrated and explained in figure 12. Farther downstream, the velocity fluctuations are over-predicted due to the delayed reattachment of the separated shear layer. The trained model substantially mitigates these issues. This significant improvement is achieved without including r.m.s. velocities in the training loss, which further demonstrates the effectiveness of the present data-driven DES model.

Figure 14 illustrates the mean skin friction coefficient C_f for flows over the bump. In the region of FPG ($0 < x/C < 0.5$), the trained model accurately predicts C_f in comparison with the LES result, while the baseline model over-predicts C_f in the region of ($0.2 < x/C < 0.5$), and the peak location of C_f is delayed in the prediction of the baseline model. In the APG region before the flow separation ($0.5 < x/C < 0.8$), there exists a local maximum of C_f for the LES results, which is also observed in previous DNS of a Gaussian bump (Balin & Jansen 2021). The existence of a local maximum is also captured by the trained model, although the magnitude is lower than the LES result. In contrast, this local maximum is not observed in the prediction of the baseline model. After the flow separation ($x/C > 0.8$), the predicted C_f by the trained model agrees well with the LES results, indicating the accurate predictions of the flow separation, reattachment of the separated shear layer and the recovery of the reattached turbulent boundary layer farther downstream. In contrast, the friction coefficient C_f predicted by the baseline model severely deviates from the LES results due to the significantly over-predicted area of the separation region, as shown in figure 12(*d–f*).

https://doi.org/10.1017/jfm.2025.11022 Published online by Cambridge University Press

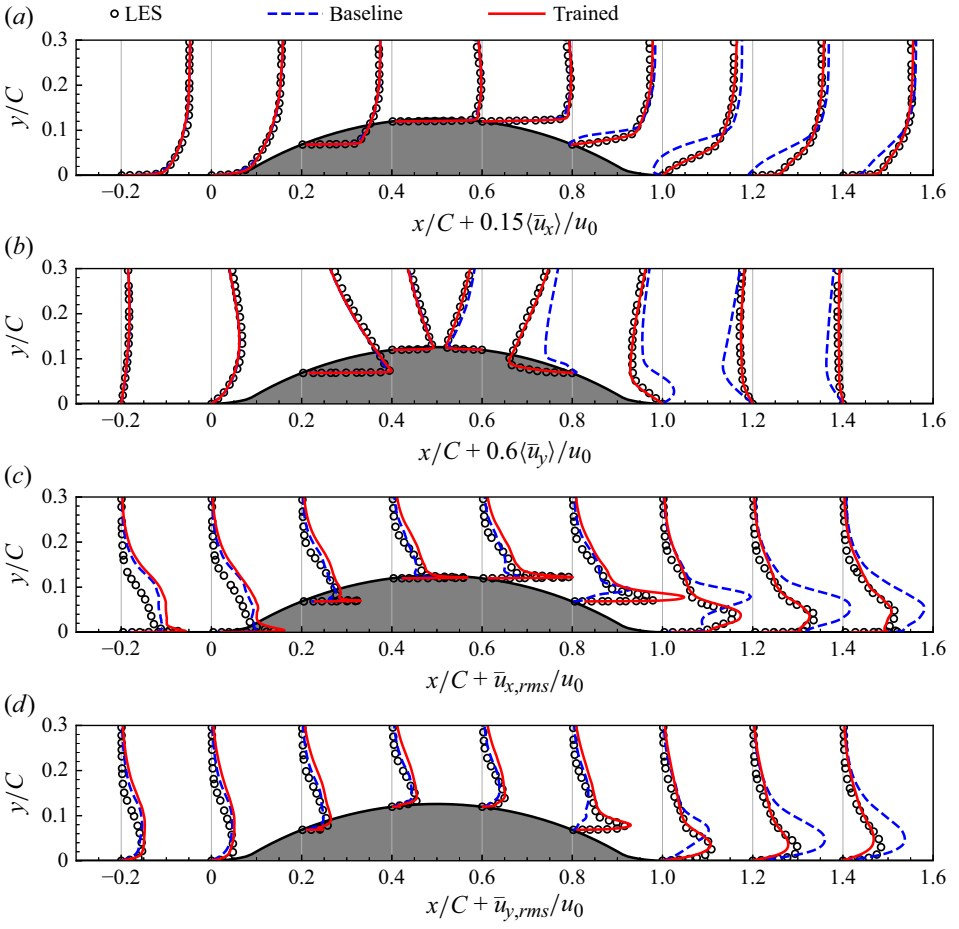


Figure 13. Comparisons of the mean and r.m.s. velocity profiles of the bump case between the LES, the baseline EAS-DDES model and the trained DD-EAS-DDES model at different streamwise locations with an interval of $0.2C$.

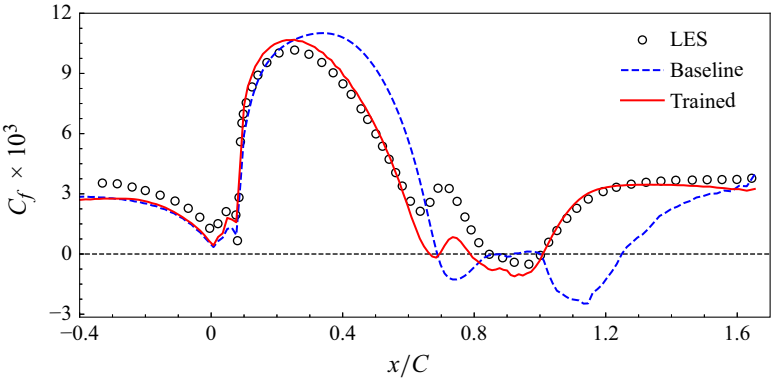


Figure 14. Comparisons of the skin friction coefficient between the LES, the baseline EAS-DDES model and the trained DD-EAS-DDES model for flows over the bump.

https://doi.org/10.1017/jfm.2025.11022 Published online by Cambridge University Press

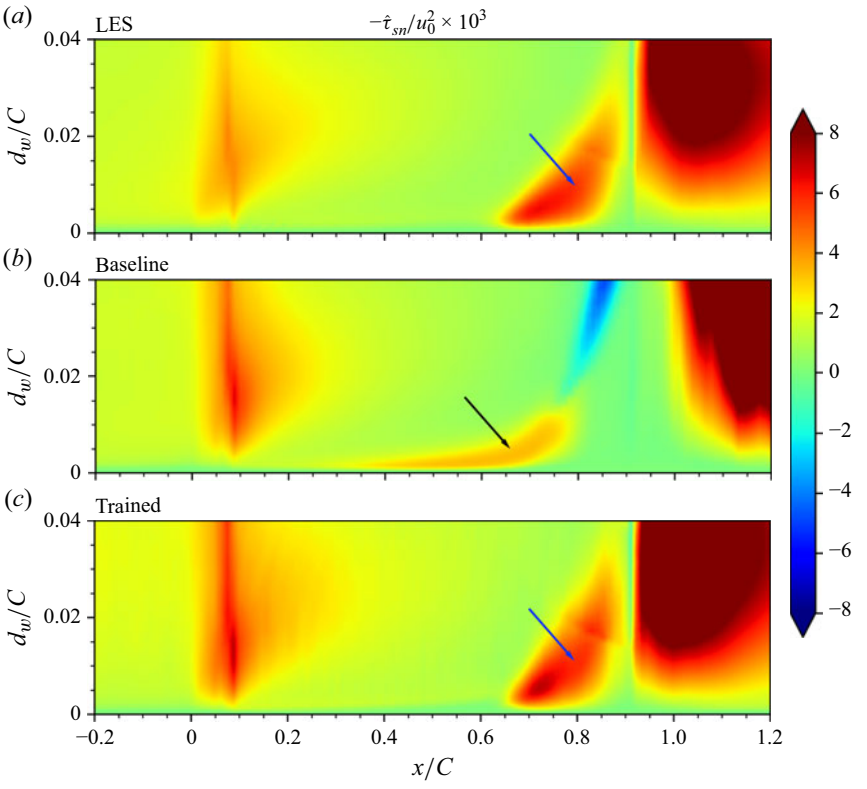


Figure 15. Comparisons of the Reynolds shear stress in the wall-frame between the LES, the baseline EAS-DDES model and the trained DD-EAS-DDES model for flows over the bump.

The improvement of the predicted mean C_f can be explained by the prediction of the turbulent stress. Based on mean friction drag decomposition in the turbulent boundary layer (Renard & Deck 2016; Fan *et al.* 2020; Elnahhas & Johnson 2022), the contributions of the mean C_f consist of a laminar part, turbulent momentum flux, streamwise growth of the boundary layer, mean wall-normal flux and the free stream pressure gradient. In consideration of the pressure gradient contribution, the free stream FPG and APG increase and decrease the mean C_f by increasing and decreasing the free stream velocity, respectively, relative to the local boundary layer. This determines the variation of mean C_f over the bump as shown in figure 14. The turbulent momentum flux contribution is determined by the turbulent shear stress in the wall frame $\hat{\tau}_{tn} \equiv \langle u_t' u_n' \rangle$, where the subscripts '$t$' and '$n$' denote the wall-tangential and wall-normal directions, respectively. In general, the increase of $\hat{\tau}_{tn}$ leads to the increase of the mean C_f.

Figure 15 depicts the distribution of $\hat{\tau}_{tn}$ under the local wall frame in the near-wall region. In the range of $0 < x/C < 0.2$, both models predict a slightly higher value of $\hat{\tau}_{tn}$ compared with the LES results. In $0.2 < x/C < 0.6$, the trained model predicts a low magnitude of $\hat{\tau}_{tn}$ near the wall due to the presence of the FPG, which is close to the LES result. However, the baseline model predicts a much higher $-\hat{\tau}_{tn}$ in this region (marked by the black arrow), resulting in an overestimated mean C_f in this region. Farther downstream, the prediction of the trained model is similar to the LES results. A high turbulent shear stress region appears in the range of $0.6 < x/C < 0.9$ due to the strong APG effect, as marked by the blue arrows. This leads to the abrupt increase of mean C_f and the occurrence of a local maximum, as shown in figure 14. The occurrence of this

https://doi.org/10.1017/jfm.2025.11022 Published online by Cambridge University Press

high $-\hat{\tau}_{tn}$ region is slightly delayed for the trained model compared with the LES result, leading to the slightly delayed increase of the mean C_f. The high $-\hat{\tau}_{tn}$ region enables the near-wall flows to resist the strong APG and keep attached until $x/C \approx 0.8$. As for the baseline model, the magnitude of $\hat{\tau}_{tn}$ in the range $0.6 < x/C < 0.8$ is significantly under-predicted, leading to premature flow separation. Overall, the baseline model fails to accurately reflect the effect of the pressure gradient on Reynolds shear stress, resulting in inaccurate predictions of the separation point and the mean C_f. In contrast, the trained model significantly improves the prediction of Reynolds shear stress, resulting in enhanced prediction performance.

5.3. *Switching behaviours and model coefficients*

Figure 16(*a*,*b*) compares the mean shielding function $\langle f_d \rangle$ of the baseline and the trained models. Similar to the square duct case, the trained model reduces the near-wall shielded RANS layer in the region over the bump ($x/C < 1$). As explained in § 4.3, $f_d = 1$ does not necessarily mean the model is switched to LES, and this is true for the present case due to a moderate mesh resolution ($\Delta x^+ \approx 100$ and $\Delta z^+ \approx 40$). Given this, we define the LES mode indicator ϕ as

$$\phi = \frac{\ell_{DDES} - \ell_{RANS}}{\ell_{LES} - \ell_{RANS}}, \tag{5.1}$$

to further demonstrate the switching behaviour. This indicator ϕ varies from 0 to 1, with $\phi = 0$ and 1 corresponding to the use of RANS or LES length scale for ℓ_{DDES}, respectively.

The mean value of ϕ is shown in figure 16(*c*,*d*). In the region before the flow separation ($x/C < 0.7$), the trained model has a higher value of $\langle \phi \rangle$ than the baseline model. This means that the trained model tends to resolve a larger proportion of turbulence scales to better predict the local turbulent state, yielding a significant improvement in the skin friction on the hump, as previously shown in figure 14. More importantly, the convection of resolved turbulent structures into the near-wall boundary layer enhances its resistance against strong APG, resulting in delayed flow separation and a more accurate separation point prediction. In figure 16(*f*), a clear, near-wall RANS layer is established after $x/C = 1.0$, which results in a good skin friction prediction after reattachment, as shown in figure 14.

Further, the resolved and modelled parts of the Reynolds shear stress are illustrated in figure 17. The solid line roughly indicates the RANS/LES switching location. For the baseline model, the near-wall RANS region is relatively thick. Moreover, the Reynolds shear stress in $0.2 < x/C < 0.6$ is over-predicted (pointed by the blue arrow in figure 17*c*), which can be attributed to the modelling error of the RANS branch in capturing the effects of the pressure gradient on the Reynolds stress. For the trained model, the near-wall flow in $0.2 < x/C < 0.6$ is largely resolved, and the effects of the pressure gradient can be effectively captured. Farther downstream, the strong APG significantly enhances the turbulent intensity, leading to an abrupt thickening of the near-wall RANS region. Before the separation ($0.6 < x/C < 0.8$), the proportion of the modelled stress played a crucial role in the total stress, as pointed by the red arrow in figure 17(*f*). This indicates that the near-wall RANS model has non-negligible contributions to the improved prediction of the flow separation point in this case.

The trained model coefficients C_1, C_2 and C_{DES}, and the calculated C_μ^* are examined for this case to explain the model behaviour. The relative variations of the trained coefficients compared with the baseline values are shown in figure 18. The value of $\langle C_{DES} \rangle$ is lower than the baseline value in the near-wall region before the separation ($x/C < 0.7$). A smaller $\langle C_{DES} \rangle$ predicted by the trained model leads to decreased subgrid viscosity (plotted

https://doi.org/10.1017/jfm.2025.11022 Published online by Cambridge University Press

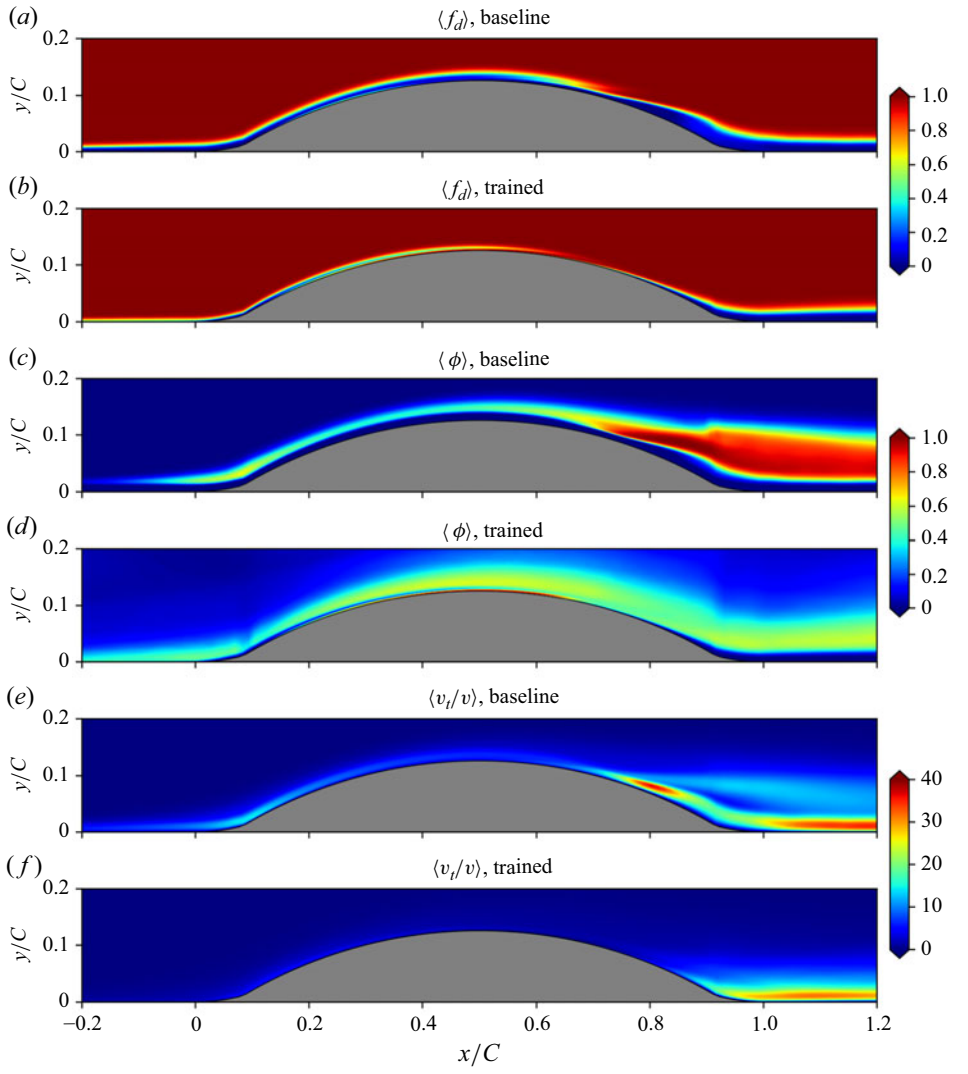


Figure 16. Comparisons of the (*a*,*b*) mean DES shielding function $\langle f_d \rangle$, (*c*,*d*) the LES mode indicator $\langle \phi \rangle$ and (*e*,*f*) the turbulent viscosity ratio $\langle \nu_t \rangle / \nu$ between the baseline EAS-DDES model and the trained DD-EAS-DDES model for flows over the bump.

in figure 16), and thus reduces the production of k near the edge of the RANS region. The variation of k can affect the RANS region thickness due to the dependency of f_d on k as in (2.7). This is the main reason for the reduction of the near-wall shielded RANS region. Additionally, the mean C_μ^* is larger than the baseline value in the whole domain through the variations in C_1 and C_2 from their baseline values. This modification to the near-wall RANS model can play an important role in the strong APG region, due to the abrupt thickening of the near-wall RANS region and the increase in the modelled stress contribution, as demonstrated in figure 17. The relatively large C_μ^* increases the near-wall shear stress in this region, enabling the flow to resist the APG and keep attached until the correct separation point. To summarize, the combined modifications of C_{DES} and C_μ^* (modified through C_1 and C_2) lead to the effective response of the near-wall shear stress to the pressure gradient by enlarging the LES region in the FPG region and modifying

https://doi.org/10.1017/jfm.2025.11022 Published online by Cambridge University Press

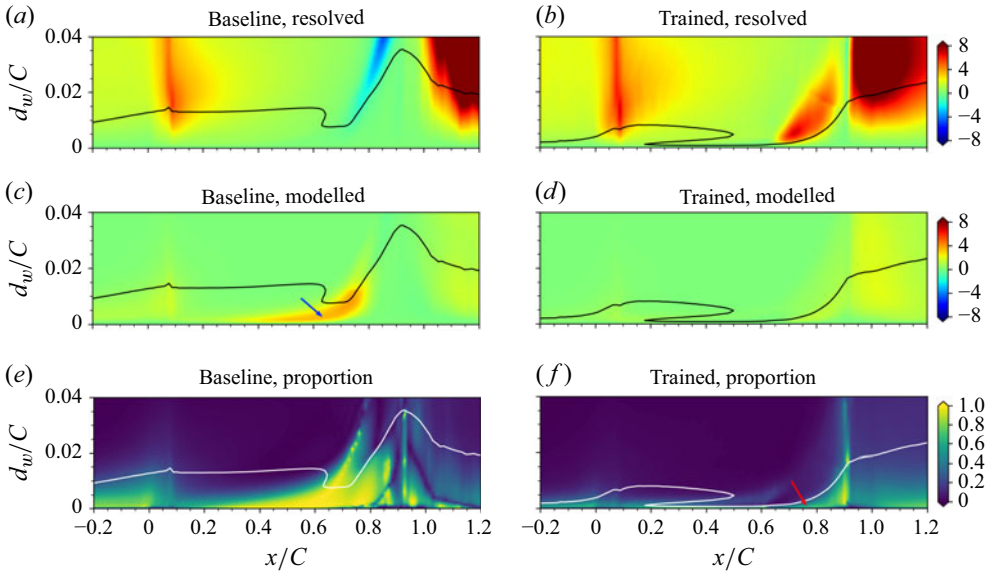


Figure 17. Comparisons of the resolved and modelled Reynolds shear stress ($\langle \bar{u}_t' \bar{u}_n' \rangle / u_0^2 \times 10^3$ and $\langle \tau_{tn} \rangle / u_0^2 \times 10^3$) in the wall-frame and the proportion of the modelled part $|\langle \tau_{tn} \rangle| / (|\langle \bar{u}_t' \bar{u}_n' \rangle| + |\langle \tau_{tn} \rangle|)$ between the LES, the baseline EAS-DDES model and the trained DD-EAS-DDES model. The solid line is the contour line of $\langle f_d \rangle = 0.5$.

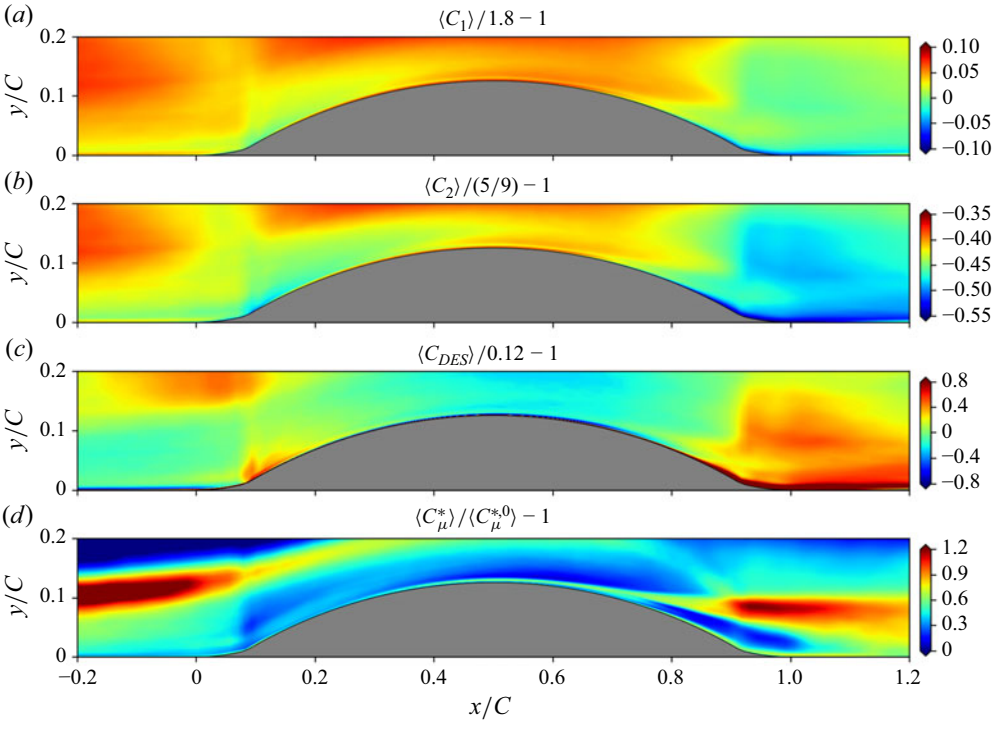


Figure 18. Mean values of the model coefficients $\langle C_1 \rangle$, $\langle C_2 \rangle$, $\langle C_{DES} \rangle$ and $\langle C_\mu^* \rangle$ of the trained DD-EAS-DDES model.

https://doi.org/10.1017/jfm.2025.11022 Published online by Cambridge University Press

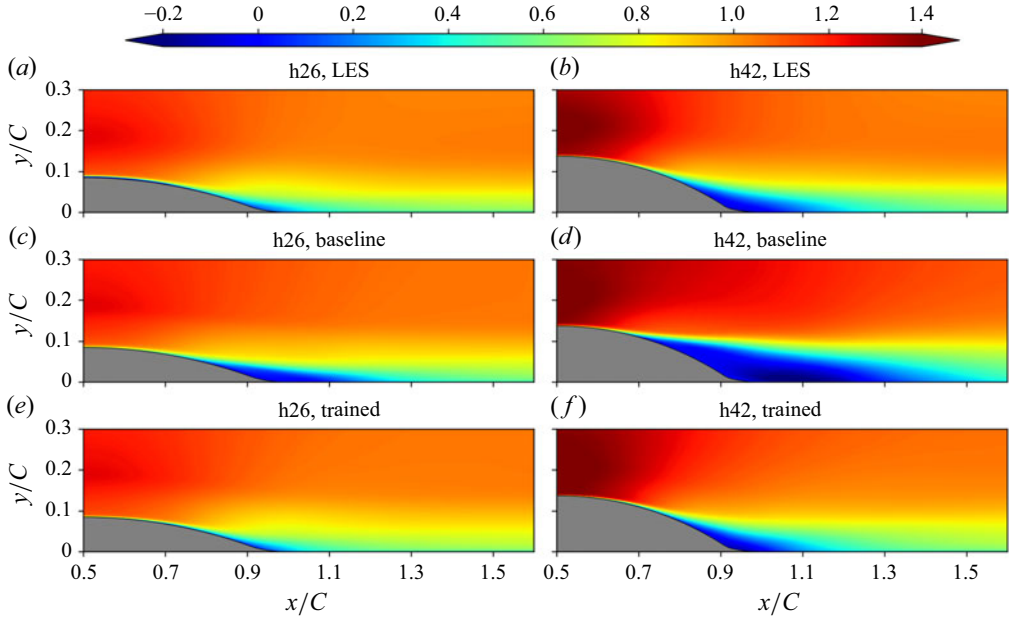


Figure 19. Comparisons of the normalized mean streamwise velocity $\langle \bar{u}_x \rangle / u_0$ contours of the flow over the bump between (*a*,*b*) the LES, (*c*,*d*) the baseline EAS-DDES model and (*e*,*f*) the trained DD-EAS-DDES model for the h26 and the h42 bumps. The DD-EAS-DDES model is trained in the h38 bump case.

the RANS model in the APG region, which improves the model prediction of the flow separation point and the skin friction.

5.4. *Generalization in similar geometries and different grid resolutions*

The generalizability of the trained model is further examined by simulating flows over the bumps with different heights. Two different bump heights, i.e. $h = 26$ and 42 mm, are chosen, denoted by the h26 and h42 cases, respectively. The h26 case is marked as the 'flow on verge of separation' in the LES of Matai & Durbin (2019*b*). The flows over the two bumps are simulated using the baseline and trained models, respectively, compared with the LES results. The employed trained model is trained from the h38 case with the bump height $h = 38$ mm. The mesh quality is kept the same as the training case.

Figure 19 illustrates the normalized mean streamwise velocity $\langle \bar{u}_x \rangle / u_0$. It can be observed that the baseline model predicts a premature separation and a delayed flow reattachment for both cases, which is similar to the observed features in the h38 case. The trained model predicts very similar flow patterns as the LES results for both cases. The separation and reattachment points of the h42 case are correctly predicted. The flow features on the verge of separation for the h26 case are also accurately captured with the trained model.

Figure 20 presents the predicted mean shielding function $\langle f_d \rangle$ and LES mode indicator $\langle \phi \rangle$ contours for the h26 and h42 bumps. These results closely match the performance observed in the training case (the h38 bump, shown in figure 16*b*,*d*). Therefore, the switching behaviour of the trained DD-EAS-DDES model can be generalized to geometrically similar configurations.

In addition, the trained model's generalizability has been assessed on a finer mesh, with the cell sizes halved in both the streamwise and spanwise directions, corresponding to $\Delta x^+ \approx 50$ and $\Delta z^+ \approx 20$ in the bump region. The cell size in the wall-normal direction is maintained. The DES is performed with the baseline and the trained models, where the

https://doi.org/10.1017/jfm.2025.11022 Published online by Cambridge University Press

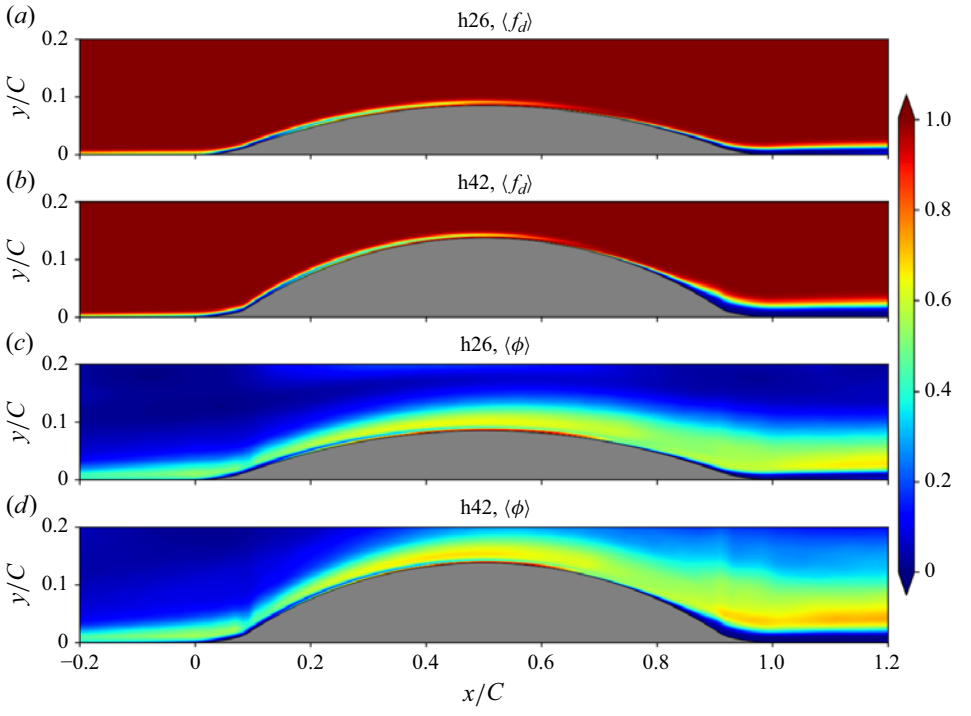


Figure 20. The mean shielding function $\langle f_d \rangle$ and LES mode indicator $\langle \phi \rangle$ contours simulated by the trained DD-EAS-DDES model for the h26 and the h42 bumps. The DD-EAS-DDES model is trained in the h38 bump case.

latter is trained on the base mesh. The mean velocity profiles are depicted in figure 21. Similar to the base-mesh results, the trained model performs significantly better compared with the baseline model on the fine mesh, indicating the robustness of the trained DD-EAS-DDES approach under different mesh resolutions. It is also worth noting that for the trained model, the fine-mesh results are relatively less accurate than those on the base mesh, as shown in figure 13(*a*,*b*). This could be further improved by training the model with different mesh resolutions.

The switching behaviours of the trained model under different mesh resolutions are demonstrated in figure 22. The mesh resolution has negligible influence on the DDES shielding function f_d. It is reasonable because the shielded RANS region is already very thin, especially on the bump surface. Since switching too close to the wall would cause premature separation, the trained model seems to sustain a robust shielding for the RANS region. In contrast to f_d, the LES mode indicator $\langle \phi \rangle$ reflects the local proportion of the resolved turbulent scales. With finer meshes, the LES mode is more prone to be activated outside the near-wall shielded region due to the decrease of ℓ_{LES}. This trend is well demonstrated by the plot of $\langle \phi \rangle$ in figure 22(*c*,*d*). Therefore, the trained model has a physically justified switching behaviour in the DDES framework.

6. Discussion

6.1. *Physical realizability*

The present model is formulated based on the algebraic equation of the modelled stress anisotropy, which ensures that the obtained modelled stress satisfies the weak-equilibrium

https://doi.org/10.1017/jfm.2025.11022 Published online by Cambridge University Press

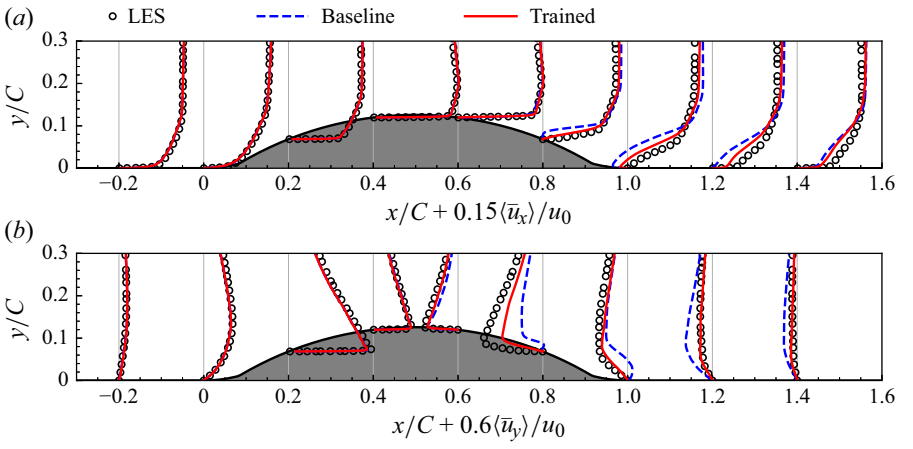


Figure 21. Comparisons of the mean velocity profiles of the bump case between the LES, the baseline EAS-DDES model and the trained DD-EAS-DDES model at different streamwise locations with an interval of $0.2C$. The DES cases are under the fine mesh, while the trained model is trained with the base mesh.

assumption. This is found to be a reasonable approximation of the full differential Reynolds stress transport equations in various flow scenarios (Wallin & Johansson 2000). Hence, in the DD-EAS-DDES model, the obtained modelled stress incorporates the physical constraint of the algebraic stress equation, which captures the physical process of the local turbulence under the weak-equilibrium assumption. In contrast, conventional neural network-based models do not embed such physical constraints, such as the tensor basis neural network (TBNN) model, where the neural network represents the mapping from the flow features to the tensor basis coefficients β_i.

One advantage of the inherent physical constraint in the DD-EAS-DDES model is the satisfaction of physical realizability. The EARS model (Wallin & Johansson 2000) is primarily formulated from the algebraic Reynolds stress equation using the LRR model (Launder *et al.* 1975) for the pressure–strain rate terms. The LRR model is known to satisfy weak realizability in all but pathologic circumstances (Durbin & Speziale 1994; Pope 2000), and the current model inherits this desirable property. Regarding the trained model, the regularization applied to the coefficients C_1, C_2 and C_{DES}, as described in § 3.2, ensures that these values do not deviate significantly from those of the baseline model. This also helps the trained model to preserve the realizability from the baseline model.

The realizability behaviour is demonstrated in figure 23 for the square duct and the bump cases simulated by the trained model. The data points on a homogeneous plane for both cases are plotted in barycentric coordinates coloured by the mean shielding function $\langle f_d \rangle$, where the barycentric triangle encloses all physically realizable states (Banerjee *et al.* 2007). For the bump case, only one-fifth of the points are plotted for clarity. It can be seen that all the points fall inside the barycentric triangle. The physical realizability of the simulated state of turbulent stress by the trained DD-EAS-DDES model in both LES and RANS branches is verified. For other modelling approaches, extra regularization has to be introduced during the training process to ensure physical realizability (Jiang *et al.* 2021).

6.2. *Training efficiency*

Using the EAS-based turbulence model as the baseline can facilitate training efficiency with improved accuracy. The LEV model is typically considered the baseline or initialized model before training for many data-driven turbulence models. For instance, in the

https://doi.org/10.1017/jfm.2025.11022 Published online by Cambridge University Press

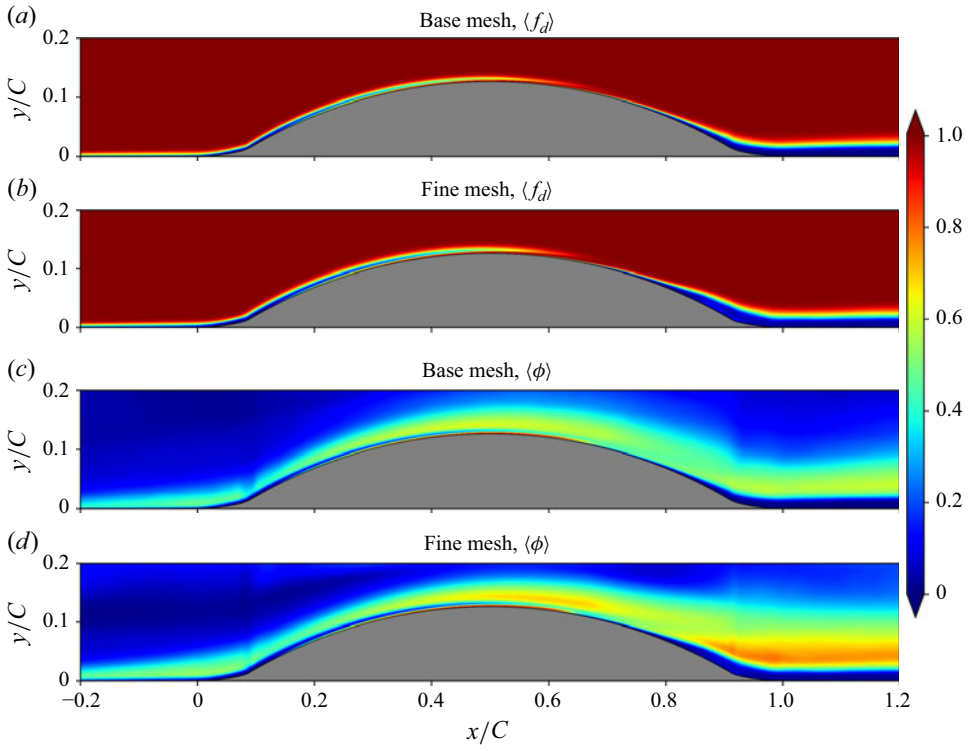


Figure 22. The mean shielding function $\langle f_d \rangle$ and LES mode indicator $\langle \phi \rangle$ contours simulated by the trained DD-EAS-DDES model for different mesh resolutions. The DD-EAS-DDES model is trained with the base mesh.

TBNN model, the initial weights are typically set to ensure $C_\mu^* = 0.09$ and $\beta_i = 0 \quad (i = 2, \ldots, 10)$ (Zhang *et al.* 2022). This corresponds to the conventional LEV-RANS models, e.g. standard $k-\varepsilon$ or $k-\omega$ models, or a corresponding LEV-DES model if the TBNN framework is adopted in formulating a data-driven DES model. The nonlinear component of the modelled stress is ignored in the initialized model and has to be developed from scratch with the data-driven method. In contrast, the present approach uses the baseline EAS-DDES model to initialize the neural network weights. The superiority of this model in predictive accuracy compared with the LEV-DES models has been demonstrated (Liu *et al.* 2024*b*). The nonlinear component of the modelled stress is inherently accounted for and can be further modified efficiently to achieve better accuracy through the modification of C_1, C_2 and C_{DES} during the training process. Therefore, the present algebraic stress-based approach can produce a trained model with better efficiency than models initialized as LEV models.

Another obvious advantage of the present approach is that the number of neural network weights required to be trained is relatively small. Although the modelled stress includes 10 tensor bases, only three model coefficients are required to be trained, and the 10 tensor basis coefficients β_i can be obtained by solving the algebraic equation of the modelled stress anisotropy. This is in contrast to the TBNN model, where the 10 tensor basis coefficients are required to be trained for the most general form of the modelled stress anisotropy. In the RANS framework, the tensor basis coefficients can be reduced to only two for statistically two-dimensional flows (Pope 2000), while this simplicity cannot be inherited in the eddy-resolved simulations, e.g. DES for the present study, due

https://doi.org/10.1017/jfm.2025.11022 Published online by Cambridge University Press

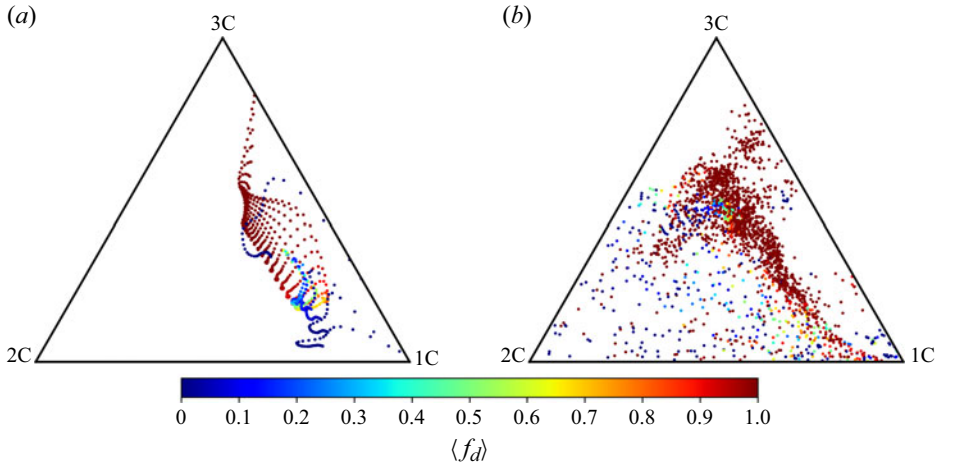


Figure 23. The local state of the Reynolds stress anisotropy in the Barycentric triangle for (*a*) the square duct flow and (*b*) the flow over the bump. The points are coloured by the mean DES shielding function $\langle f_d \rangle$.

to the three-dimensional nature of turbulence. Hence, the present approach can reduce the neural network weights to achieve improved training efficiency.

6.3. *Computational efficiency*

The present DD-EAS-DDES model computes the Reynolds stress anisotropy from algebraic formulations and uses a neural network to represent the model coefficients, without introducing extra transport equations. Hence, the present model maintains the computational efficiency of the baseline EAS-DDES model, or any existing $k-\omega$ based DES approaches, which is significantly less costly than the WRLES or DNS. Specifically, for the present simulation of the flow over a bump, the mesh resolution is $\Delta x^+ \approx 100$ and $\Delta z^+ \approx 40$ in the bump region, which is approximately three times coarser per direction than the WRLES (Matai & Durbin 2019*b*), and six times coarser in wall units than the DNS in a similar case (Balin & Jansen 2021). Considering the related requirement of the time step size, the present DD-EAS-DDES reduces the computational cost by factors of 30 and 300 compared with the corresponding WRLES and DNS, respectively. Furthermore, the near-wall RANS behaviour for DES largely relaxes the wall-normal cell spacing requirement compared with LES and DNS, leading to further reduction of the computational cost.

As another illustration, Spalart (2000) provided a rough estimation of the computational cost for different turbulence simulation strategies. The targets are high-Reynolds-number external flows typical of commercial aircraft and ground vehicles. The evaluated computational costs for DES, LES and DNS, in terms of spatial and temporal degrees of freedom, are 10^{12}, $10^{18.2}$ and $10^{23.7}$, respectively. This highlights the advantage of DES in computational efficiency over LES or DNS for practical applications.

7. Conclusion

In the present work, a data-driven DES method based on the algebraic stress equation is proposed. The modelled stress in the DES is formulated as the summation of the linear and nonlinear parts. The linear part is responsible for the switching between the RANS and LES branches through the eddy viscosity ν_t, based on the $\ell^2-\omega$ framework.

https://doi.org/10.1017/jfm.2025.11022 Published online by Cambridge University Press

The nonlinear part introduces additional anisotropy to the modelled stress. The modelled stress anisotropy is expressed as the tensor basis form, with the tensor basis coefficients β_i obtained by solving the algebraic equation of the modelled stress anisotropy under the weak-equilibrium assumptions. There exist three model coefficients, i.e. C_1 and C_2 for the slow and rapid pressure–strain rate terms in the algebraic stress equation, and C_{DES} in the LES length scale. These coefficients are formulated as functions of the scalar invariants θ_i, represented with the neural network. The neural network is trained by the ensemble Kalman method with velocity data, circumventing the need to provide the modelled stress data. Moreover, to ensure a similar RANS/LES switching behaviour as the baseline model, the model coefficients C_1, C_2 and C_{DES} are augmented to the observation space, with the baseline values treated as the reference data.

The capability of the proposed framework is illustrated in two challenging turbulent flows: the secondary flow in a square duct and the separated flow over a bump. The former is characterized by significant Reynolds stress anisotropies that induce secondary motions, and the latter is featured by strong pressure gradients in the turbulent boundary layer and the flow separation on a curved surface. The DNS for the square duct case and the WRLES for the bump case are used as the training data. For both cases, the trained model achieves significant improvements compared with the baseline model in predicting the mean flow statistics, including mean velocity and skin friction coefficient. Such improvements are mainly attributed to the improved modelled stress. Moreover, reasonable switching behaviour between the RANS and LES modes is obtained, where the trained model tends to enlarge the LES region to resolve more turbulent structures. The distributions of the trained model coefficients C_1, C_2 and C_{DES} are analysed to explain the model behaviour. The combined effects of the adaptive C_{DES} and C_μ^* (controlled by C_1 and C_2) contribute to the expansion of the LES region. It is also observed that the adaptive coefficients improve the modelled stress predictions on both the RANS and LES branches. The generalizability of the trained model is further examined by simulating the square duct flow at a relatively high Reynolds number and the bump flow with different crest heights. The predictions of the trained model in all these cases are in better agreement with the DNS or WRLES results, compared with the baseline model.

A main limitation of this study is that two distinct turbulence models (with the same structure but different neural network weight parameters $\boldsymbol{w}$) are trained separately for two different flow cases, rather than developing a single, universal turbulence model applicable to a broader range of scenarios. We note that the primary objective of this work is to establish a data-driven framework for DES based on the algebraic stress equation. Therefore, the development of a unified model across multiple cases is not pursued here. This work serves as a foundational step towards integrating data-driven methods with DES, and extending the framework to handle multiple flow configurations will be the focus of future investigation. Future work will also focus on generalizing the data-driven DES model to significantly different Reynolds numbers and geometries from the training data. Special attention will be paid to the model's switching behaviour during the generalization, and the consistency and convergence behaviours of the RANS-to-LES interface will be rigorously examined.

Another potential concern regarding the current DD-EAS-DDES approach is its relatively high training cost. This work primarily focuses on establishing a novel data-driven DES framework. While reducing the training expense of a three-dimensional, unsteady data-driven turbulence model remains an important goal for future research, it is not the focus of this work. Notably, the trained model demonstrates satisfactory generalizability to flows with similar geometries and Reynolds numbers. This capability allows the initial training cost to be amortized across numerous simulations, e.g. in

https://doi.org/10.1017/jfm.2025.11022 Published online by Cambridge University Press

parametric studies or design optimization, thereby enhancing overall computational efficiency over time. Therefore, the approach can be highly cost-effective for long-term use.

Acknowledgements. This work is supported by NSFC, the Excellence Research Group Program for multiscale problems in nonlinear mechanics (grant no. 12588201). H.-C. Liu also acknowledges support from the China National Postdoctoral Program for Innovative Talents (no. BX20250282) and the China Postdoctoral Science Foundation (no. 2024M763359). X.-L. Zhang acknowledges support from the Young Elite Scientists Sponsorship Program by CAST (no. 2022QNRC001) and the CAS Project for Young Scientists in Basic Research (YSBR-087). Finally, the authors gratefully acknowledge Dr R. Matai for providing the LES data of the bump case.

Declaration of interests. The authors report no conflict of interest.

Appendix A. Full expressions of the tensor basis coefficients

The solution of the algebraic (2.19) of the modelled stress anisotropy is provided here. The coefficients A_i are defined for convenience, which are related to the pressure–strain rate coefficients C_1 and C_2 as

$$A_1 = \frac{88}{15(7C_2+1)}, \quad A_2 = \frac{5-9C_2}{7C_2+1}, \quad A_3 = \frac{11(C_1-1)}{7C_2+1}, \quad A_4 = \frac{11}{7C_2+1}. \tag{A1}$$

The parameter N is defined as a function of $\mathcal{P}/\varepsilon$,

$$N = A_3 + A_4\frac{\mathcal{P}}{\varepsilon}. \tag{A2}$$

Inserting (2.8) into (2.19), the coefficients β_i can be obtained as a function of N as

$$\begin{aligned}
\beta_1 &= -\frac{1}{2}A_1N\left(30A_2\theta_4 - 21N\theta_2 - 2A_2^3\theta_3 + 6N^3 - 3A_2^2\theta_1N\right)/Q,\\
\beta_2 &= -A_1A_2\left(6A_2\theta_4 + 12N\theta_2 + 2A_2^3\theta_3 - 6N^3 + 3A_2^2\theta_1N\right)/Q,\\
\beta_3 &= -3A_1\left(2A_2^2\theta_3 + 3NA_2\theta_1 + 6\theta_4\right)/Q,\\
\beta_4 &= -A_1\left(2A_2^3\theta_3 + 3A_2^2N\theta_1 + 6A_2\theta_4 - 6N\theta_2 + 3N^3\right)/Q,\\
\beta_5 &= 9A_1A_2N^2/Q, \quad \beta_6 = -9A_1N^2/Q, \quad \beta_7 = 18A_1A_2N/Q,\\
\beta_8 &= 9A_1A_2^2N/Q, \quad \beta_9 = 9A_1N/Q, \quad \beta_{10} = 0,
\end{aligned} \tag{A3}$$

with the denominator

$$\begin{aligned}
Q = {} & 3N^5 + \left(-\frac{15}{2}\theta_2 - \frac{7}{2}A_2^2\theta_1\right)N^3 + \left(21A_2\theta_4 - A_2^3\theta_3\right)N^2\\
& + \left(3\theta_2^2 - 8A_2^2\theta_1\theta_2 + 24A_2^2\theta_5 + A_2^4\theta_1^2\right)N + \frac{2}{3}A_2^5\theta_1\theta_3\\
& + 2A_2^3\theta_4\theta_1 - 2A_2^3\theta_2\theta_3 - 6A_2\theta_4\theta_2.
\end{aligned} \tag{A4}$$

The parameter N related to the production–dissipation ratio as (A2) can be computed based on the definition of $\mathcal{P}/\varepsilon$ as (2.20). This results in a cubic equation for the two-dimensional flow and a sixth-order equation for the three-dimensional flow. As in the previous study (Liu *et al.* 2024*b*), the two-dimensional solution, as given by (A5), is used as an approximation for the three-dimensional flow here. This has been claimed to induce

https://doi.org/10.1017/jfm.2025.11022 Published online by Cambridge University Press

negligible differences to the simulation results (Wallin & Johansson 2000).

$$N = \begin{cases} \dfrac{A_3}{3} + \left(P_1 + \sqrt{P_2}\right)^{1/3} + \operatorname{sign}\left(P_1 - \sqrt{P_2}\right)\left|P_1 - \sqrt{P_2}\right|^{1/3}, & P_2 \geqslant 0 \\ \dfrac{A_3}{3} + 2\left(P_1^2 - P_2\right)^{1/6} \cos\left(\dfrac{1}{3}\arccos\left(\dfrac{P_1}{\sqrt{P_1^2 - P_2}}\right)\right), & P_2 < 0 \end{cases} \tag{A5}$$

where

$$\begin{aligned} P_1 &= \left[\frac{A_3^2}{27} + \left(\frac{A_1 A_4}{6} - \frac{2}{9}A_2^2\right)\theta_1 - \frac{2}{3}\theta_2\right] A_3, \\ P_2 &= P_1^2 - \left[\frac{A_3^2}{9} + \left(\frac{A_1 A_4}{3} + \frac{2}{9}A_2^2\right)\theta_1 + \frac{2}{3}\theta_2\right]^3. \end{aligned} \tag{A6}$$

The algebraic equation of $\boldsymbol{a}$ requires correction to obtain a reasonable value of C_μ^* at small $\mathcal{P}/\varepsilon$, where the advection and diffusion of $\boldsymbol{a}$ are non-negligible. In analogy to the approach of (Wallin & Johansson 2000), an effective diffusion term $\boldsymbol{D}^*$ is added to the right-hand side of (2.13) as the correction, which reads

$$\boldsymbol{D}^* = C_D \boldsymbol{a} \boldsymbol{\nabla} \cdot \boldsymbol{T}_k, \tag{A7}$$

where $\boldsymbol{T}_k$ is the flux of TKE. Considering the balance of the k-equation, we have

$$\boldsymbol{\nabla} \cdot \boldsymbol{T}_k \approx \mathcal{P} - \varepsilon. \tag{A8}$$

Insert it into (2.19), estimate $\mathcal{P}/\varepsilon$ by $-\beta_1^{eq}\theta_1$ and switch off the correction at $\mathcal{P}/\varepsilon > 1$. Afterward, the correction of A_3 is obtained as

$$A_3' = A_3 + \frac{11}{7C_2 + 1} C_D \max\left(1 + \beta_1^{eq}\theta_1, 0\right) \tag{A9}$$

where β_1^{eq} is the value of β at $\mathcal{P} = \varepsilon$. It is estimated by the expression in a two-dimensional condition as

$$\beta_1^{eq} = -\frac{A_1 N^{eq}}{(N^{eq})^2 - 2\theta_2 - (2/3)A_2^2\theta_1}, \tag{A10}$$

where $N^{eq} = A_3 + A_4$ is the value of N at $\mathcal{P} = \varepsilon$. As for the effective diffusion coefficient C_D, it is determined by the condition of $C_\mu^* = C_\mu$ at zero strain rates. The final expression is

$$C_D = \frac{4}{15C_\mu} - C_1 + 1. \tag{A11}$$

References

Abadi, M., *et al.* 2016 TensorFlow: Large-scale machine learning on heterogeneous systems. arXiv: 1603.04467.

Ashton, N., Revell, A., Prosser, R. & Uribe, J. 2013 Development of an alternative delayed detached-eddy simulation formulation based on elliptic relaxation. *AIAA J.* **51** (2), 513–519.

Bader, S.H., Yin, Z. & Durbin, P.A. 2022 A hybrid model for turbulence and transition, with a locally varying coefficient. *Flow Turbul. Combust.* **108** (4), 935–954.

Balin, R. & Jansen, K.E. 2021 Direct numerical simulation of a turbulent boundary layer over a bump with strong pressure gradients. *J. Fluid Mech.* **918**, A14.

Banerjee, S., Krahl, R., Durst, F. & Zenger, C. 2007 Presentation of anisotropy properties of turbulence, invariants versus eigenvalue approaches. *J. Turbul.* **8**, N32.

https://doi.org/10.1017/jfm.2025.11022 Published online by Cambridge University Press

BOSE, R. & ROY, A.M. 2024 Invariance embedded physics-infused deep neural network-based sub-grid scale models for turbulent flows. *Engng Applics Artif. Intell.* **128**, 107483.
BRUNTON, S.L., NOACK, B.R. & KOUMOUTSAKOS, P. 2020 Machine learning for fluid mechanics. *Annu. Rev. Fluid Mech.* **52** (1), 477–508.
CHAOUAT, B. 2017 The state of the art of hybrid RANS/LES modeling for the simulation of turbulent flows. *Flow Turbul. Combust.* **99**, 279–327.
DECK, S. 2012 Recent improvements in the zonal detached eddy simulation (ZDES) formulation. *Theor. Comput. Fluid Dyn.* **26**, 523–550.
DURAISAMY, K. 2021 Perspectives on machine learning-augmented Reynolds-averaged and large eddy simulation models of turbulence. *Phys. Rev. Fluids* **6** (5), 050504.
DURAISAMY, K., IACCARINO, G. & XIAO, H. 2019 Turbulence modeling in the age of data. *Annu. Rev. Fluid Mech.* **51**, 357–377.
DURBIN, P.A. 2011 *Statistical Theory and Modeling for Turbulent Flows*. Wiley Sons Ltd.
DURBIN, P.A. & SPEZIALE, C.G. 1994 Realizability of second-moment closure via stochastic analysis. *J. Fluid Mech.* **280**, 395–407.
DURBIN, P.A. 2018 Some recent developments in turbulence closure modeling. *Annu. Rev. Fluid Mech.* **50** (1), 77–103.
ELNAHHAS, A. & JOHNSON, P.L. 2022 On the enhancement of boundary layer skin friction by turbulence: an angular momentum approach. *J. Fluid Mech.* **940**, A36.
EVENSEN, G. 2009 *Data Assimilation: The Ensemble Kalman Filter*. Springer.
FAN, Y., LI, W., ATZORI, M., POZUELO, R., SCHLATTER, P. & VINUESA, R. 2020 Decomposition of the mean friction drag in adverse-pressure-gradient turbulent boundary layers. *Phys. Rev. Fluids* **5** (11), 114608.
FANG, Y., ZHAO, Y., WASCHKOWSKI, F., OOI, A.S.H. & SANDBERG, R.D. 2023 Toward more general turbulence models via multicase computational-fluid-dynamics-driven training. *AIAA J.* **61** (5), 2100–2115.
GATSKI, T.B. & JONGEN, T. 2000 Nonlinear eddy viscosity and algebraic stress models for solving complex turbulent flows. *Prog. Aerosp. Sci.* **36** (8), 655–682.
GRITSKEVICH, M.S., GARBARUK, A.V., SCHÜTZE, J. & MENTER, F.R. 2012 Development of DDES and IDDES formulations for the k-ω shear stress transport model. *Flow Turbul. Combust.* **88**, 431–449.
HAN, Y., HE, Y. & LE, J. 2020 Modification to improved delayed detached-eddy simulation regarding the log-layer mismatch. *AIAA J.* **58** (2), 712–721.
HARRIS, V.G., GRAHAM, J.A.H. & CORRSIN, S. 1977 Further experiments in nearly homogeneous turbulent shear flow. *J. Fluid Mech.* **81** (4), 657–687.
HEINZ, S. 2020 A review of hybrid RANS-LES methods for turbulent flows: concepts and applications. *Prog. Aerosp. Sci.* **114**, 100597.
JASAK, H., *et al.* 2007 OpenFOAM: a C++ library for complex physics simulations. In *International Workshop on Coupled Methods in Numerical Dynamics*, pp. 1–20. IUC Dubrovnik Croatia.
JEE, S.K. & SHARIFF, K. 2014 Detached-eddy simulation based on the v2-f model. *Intl J. Heat Fluid Flow* **46**, 84–101.
JIANG, C., VINUESA, R., CHEN, R., MI, J., LAIMA, S. & LI, H. 2021 An interpretable framework of data-driven turbulence modeling using deep neural networks. *Phys. Fluids* **33** (5), 055133.
KLEIN, M., SADIKI, A. & JANICKA, J. 2003 A digital filter based generation of inflow data for spatially developing direct numerical or large eddy simulations. *J. Comput. Phys.* **186** (2), 652–665.
LAUNDER, B.E., REECE, G.J. & RODI, W. 1975 Progress in the development of a Reynolds-stress turbulence closure. *J. Fluid Mech.* **68** (3), 537–566.
LE PAPE, A., RICHEZ, F. & DECK, S. 2013 Zonal detached-eddy simulation of an airfoil in poststall condition. *AIAA J.* **51** (8), 1919–1931.
LI, Q., CHEN, X., WANG, G. & LIU, Y. 2022 A dynamic version of the improved delayed detached-eddy simulation based on the differential Reynolds-stress model. *Phys. Fluids* **34** (11), 115112.
LILLY, D.K. 1991 A proposed modification of the Germano subgrid-scale closure method. *Phys. Fluids A: Fluid Dyn.* **4** (3), 633–635.
LING, J., KURZAWSKI, A. & TEMPLETON, J. 2016 Reynolds averaged turbulence modelling using deep neural networks with embedded invariance. *J. Fluid Mech.* **807**, 155–166.
LING, J. & TEMPLETON, J. 2015 Evaluation of machine learning algorithms for prediction of regions of high Reynolds averaged Navier Stokes uncertainty. *Phys. Fluids* **27** (8), 085103.
LIU, H., YIN, Z. & LIU, H. 2024*a* Adaptive detached eddy simulation of turbulent combustion with the subgrid dissipation concept. *Phys. Fluids* **36** (5), 055154.
LIU, H., ZHANG, X., YIN, Z. & HE, G. 2024*b* An explicit algebraic stress-based delayed detached eddy simulation model for turbulent flows. *AIAA J.* **63** (6), 2249–2260.

https://doi.org/10.1017/jfm.2025.11022 Published online by Cambridge University Press

LIU, J., CHEN, J. & XIAO, Z. 2024*c* Improvements for the DDES model with consideration of grid aspect ratio and coherent vortex structures. *Aerosp. Sci. Technol.* **151**, 109314.

LIU, Y., ZHOU, Z.., ZHU, L. & WANG, S. 2021 Numerical investigation of flows around an axisymmetric body of revolution by using Reynolds-stress model based hybrid Reynolds-averaged Navier–Stokes/large eddy simulation. *Phys. Fluids* **33** (8), 085115.

LOZANO-DURÁN, A. & BAE, H.J. 2023 Machine learning building-block-flow wall model for large-eddy simulation. *J. Fluid Mech.* **963**, A35.

MARSTORP, L., BRETHOUWER, G., GRUNDESTAM, O. & JOHANSSON, A.V. 2009 Explicit algebraic subgrid stress models with application to rotating channel flow. *J. Fluid Mech.* **639**, 403–432.

MATAI, R. & DURBIN, P.A. 2019*a* Zonal eddy viscosity models based on machine learning. *Flow Turbul. Combust.* **103**, 93–109.

MATAI, R. & DURBIN, P.A. 2019*b* Large-eddy simulation of turbulent flow over a parametric set of bumps. *J. Fluid Mech.* **866**, 503–525.

MICHELÉN-STRÖFER, C.A., ZHANG, X.-L. & XIAO, H. 2021 DAFI: an open-source framework for ensemble-based data assimilation and field inversion. *Commun. Comput. Phys.* **29** (5), 1583–1622.

PARK, J. & CHOI, H. 2021 Toward neural-network-based large eddy simulation: application to turbulent channel flow. *J. Fluid Mech.* **914**, A16.

PETTERSSON REIF, B.A. & ANDERSSON, H.I. 2002 Prediction of turbulence-generated secondary mean flow in a square duct. *Flow Turbul. Combust.* **68**, 41–61.

PIROZZOLI, S., MODESTI, D., ORLANDI, P. & GRASSO, F. 2018 Turbulence and secondary motions in square duct flow. *J. Fluid Mech.* **840**, 631–655.

PONT-VÍLCHEZ, A., DUBEN, A., GOROBETS, A., REVELL, A., OLIVA, A. & TRIAS, F.X. 2021 New strategies for mitigating the gray area in delayed-detached eddy simulation models. *AIAA J.* **59** (9), 3331–3345.

POPE, S.B. 1975 A more general effective-viscosity hypothesis. *J. Fluid Mech.* **72** (2), 331–340.

POPE, S.B. 2000 *Turbulent Flows*. Cambridge University Press.

PROBST, A., SCHWAMBORN, D., GARBARUK, A., GUSEVA, E., SHUR, M., STRELETS, M. & TRAVIN, A. 2017 Evaluation of grey area mitigation tools within zonal and non-zonal RANS-LES approaches in flows with pressure induced separation. *Intl J. Heat Fluid Flow* **68**, 237–247.

REDDY, K.R., RYON, J.A. & DURBIN, P.A. 2014 A DDES model with a Smagorinsky-type eddy viscosity formulation and log-layer mismatch correction. *Intl J. Heat Fluid Flow* **50**, 103–113.

RENARD, N. & DECK, S. 2016 A theoretical decomposition of mean skin friction generation into physical phenomena across the boundary layer. *J. Fluid Mech.* **790**, 339–367.

RODI, W. 1972 The prediction of free turbulent boundary layers by use of a two-equation model of turbulence. PhD Thesis, University of London, London.

ROTTA, J.C. 1951 Statistische theorie nichthomogener turbulenz. *Z. Phys.* **129**, 547–572.

SANDBERG, R.D. & ZHAO, Y. 2022 Machine-learning for turbulence and heat-flux model development: a review of challenges associated with distinct physical phenomena and progress to date. *Intl J. Heat Fluid Flow* **95**, 108983.

SCHMELZER, M., DWIGHT, R.P. & CINNELLA, P. 2020 Discovery of algebraic Reynolds-stress models using sparse symbolic regression. *Flow Turbul. Combust.* **104** (2), 579–603.

SHUR, M.L., SPALART, P.R., STRELETS, M.K. & TRAVIN, A.K. 2008 A hybrid RANS-LES approach with delayed-DES and wall-modelled LES capabilities. *Intl J. Heat Fluid Flow* **29** (6), 1638–1649.

SINGH, A.P., MEDIDA, S. & DURAISAMY, K. 2017 Machine-learning-augmented predictive modeling of turbulent separated flows over airfoils. *AIAA J.* **55** (7), 2215–2227.

SIRIGNANO, J. & MACART, J.F. 2023 Deep learning closure models for large-eddy simulation of flows around bluff bodies. *J. Fluid Mech.* **966**, A26.

SIRIGNANO, J., MACART, J.F. & FREUND, J.B. 2020 DPM: a deep learning PDE augmentation method with application to large-eddy simulation. *J. Comput. Phys.* **423**, 109811.

SPALART, P.R. 1997 Comments on the feasibility of LES for wings, and on a hybrid RANS/LES approach. In *Proceedings of First AFOSR International Conference on DNS/LES*. Greyden Press.

SPALART, P.R. 2000 Strategies for turbulence modelling and simulations. *Intl J. Heat Fluid Flow* **21** (3), 252–263.

SPALART, P.R. 2009 Detached-eddy simulation. *Annu. Rev. Fluid Mech.* **41**, 181–202.

SPALART, P.R., DECK, S., SHUR, M.L., SQUIRES, K.D., STRELETS, M.K. & TRAVIN, A. 2006 A new version of detached-eddy simulation, resistant to ambiguous grid densities. *Theor. Comput. Fluid Dyn.* **20** (3), 181.

TAULBEE, D.B. 1992 An improved algebraic Reynolds stress model and corresponding nonlinear stress model. *Phys. Fluids A: Fluid Dyn.* **4** (11), 2555–2561.

https://doi.org/10.1017/jfm.2025.11022 Published online by Cambridge University Press

VOLPIANI, P.S. 2024 Are random forests better suited than neural networks to augment RANS turbulence models? *Intl J. Heat Fluid Flow* **107**, 109348.
VREMAN, A.W. 2004 An eddy-viscosity subgrid-scale model for turbulent shear flow: algebraic theory and applications. *Phys. Fluids* **16** (10), 3670–3681.
WALLIN, S. & JOHANSSON, A.V. 2000 An explicit algebraic Reynolds stress model for incompressible and compressible turbulent flows. *J. Fluid Mech.* **403**, 89–132.
WANG, G., LI, Q. & LIU, Y. 2021 IDDES method based on differential Reynolds-stress model and its application in bluff body turbulent flows. *Aerosp. Sci. Technol.* **119**, 107207.
WANG, G., TANG, Y. & LIU, Y. 2025 Gray area mitigation in grid-adaptive simulation for wall-bounded turbulent flows. *Intl J. Mech. Sci.* **296**, 110305.
WANG, J.-X., WU, J.-L. & XIAO, H. 2017 Physics-informed machine learning approach for reconstructing Reynolds stress modeling discrepancies based on DNS data. *Phys. Rev. Fluids* **2** (3), 034603.
WU, C., ZHANG, X.-L., XU, D. & HE, G. 2025 A framework for learning symbolic turbulence models from indirect observation data via neural networks and feature importance analysis. *J. Comput. Phys.* **537**, 114068.
WU, J.-L., XIAO, H. & PATERSON, E. 2018 Physics-informed machine learning approach for augmenting turbulence models: a comprehensive framework. *Phys. Rev. Fluids* **3** (7), 074602.
WU, X. 2017 Inflow turbulence generation methods. *Annu. Rev. Fluid Mech.* **49**, 23–49.
XU, D., WANG, J., YU, C. & CHEN, S. 2023 Artificial-neural-network-based nonlinear algebraic models for large-eddy simulation of compressible wall-bounded turbulence. *J. Fluid Mech.* **960**, A4.
YIN, Z. & DURBIN, P.A. 2016 An adaptive DES model that allows wall-resolved eddy simulation. *Intl J. Heat Fluid Flow* **62**, 499–509.
YIN, Z. & DURBIN, P.A. 2022 Detached eddy simulation of transition in turbomachinery: linear compressor cascade. *J. Turbomach.* **144** (3), 031002.
YIN, Z., GE, X. & DURBIN, P. 2021 Adaptive detached eddy simulation of transition under the influence of free-stream turbulence and pressure gradient. *J. Fluid Mech.* **915**, A115.
YIN, Z., REDDY, K.R. & DURBIN, P.A. 2015 On the dynamic computation of the model constant in delayed detached eddy simulation. *Phys. Fluids* **27** (2), 025105.
ZHANG, F., ZHOU, Z., YANG, X. & HE, G. 2025 Knowledge-integrated additive learning for consistent near-wall modelling of turbulent flows. *J. Fluid Mech.* **1011**, R1.
ZHANG, X.-L., MICHELÉN-STRÖFER, C. & XIAO, H. 2020 Regularized ensemble Kalman methods for inverse problems. *J. Comput. Phys.* **416**, 109517.
ZHANG, X.-L., XIAO, H., HE, G.-W. & WANG, S.Z. 2021 Assimilation of disparate data for enhanced reconstruction of turbulent mean flows. *Comput. Fluids* **224**, 104962.
ZHANG, X.-L., XIAO, H., JEE, S. & HE, G. 2023*a* Physical interpretation of neural network-based nonlinear eddy viscosity models. *Aerosp. Sci. Technol.* **142**, 108632.
ZHANG, X.-L., XIAO, H., LUO, X. & HE, G. 2022 Ensemble Kalman method for learning turbulence models from indirect observation data. *J. Fluid Mech.* **949**, A26.
ZHANG, X.-L., XIAO, H., LUO, X. & HE, G. 2023*b* Combining direct and indirect sparse data for learning generalizable turbulence models. *J. Comput. Phys.* **489**, 112272.
ZHOU, Z., HE, G. & YANG, X. 2021 Wall model based on neural networks for LES of turbulent flows over periodic hills. *Phys. Rev. Fluids* **6** (5), 054610.
ZHOU, Z., ZHANG, X.-L., HE, G.-W. & YANG, X. 2025 A wall model for separated flows: embedded learning to improve a posteriori performance. *J. Fluid Mech.* **1002**, A3.
ZHUCHKOV, R.N. & UTKINA, A.A. 2016 Combining the SSG/LRR-ω differential Reynolds stress model with the detached eddy and laminar-turbulent transition models. *Fluid Dyn.* **51** (6), 733–744.

https://doi.org/10.1017/jfm.2025.11022 Published online by Cambridge University Press